

# Intergranular normal stress distributions in untextured polycrystalline aggregates

S. El Shawish<sup>a,\*</sup>, J. Hure<sup>b,\*</sup>

<sup>a</sup>*Jožef Stefan Institute, SI-1000, Ljubljana, Slovenia*

<sup>b</sup>*CEA, Université Paris-Saclay, DEN, Service d'Études des Matériaux Irradiés, 91191 Gif-sur-Yvette cedex, France*

---

## Abstract

From a general point of view, InterGranular Stress-Corrosion Cracking (IGSCC) results from the interplay between mechanical loading and grain boundaries opening. The former leads to intergranular stresses in polycrystalline aggregates, the latter being either stress-accelerated or stress-induced. This work aims at obtaining intergranular normal stress distributions in uncracked polycrystalline aggregates, which is considered as a key milestone towards IGSCC initiation predictive modelling. Based on the finite element method, numerical simulations have been performed on Voronoi polycrystalline aggregates considering a wide variety of material constitutive equations: crystal elasticity (cubic and hexagonal symmetries) with different anisotropy ratios and crystal plasticity for different sets of slip systems under the assumption of uniform critical resolved shear stress: Face-Centered Cubic (FCC), Body-Centered Cubic (BCC) and Hexagonal Close Packed (HCP) with or without hardening, and for both uniaxial and equibiaxial macroscopic loading conditions. In the elastic regime, a correlation between standard deviations of intergranular normal stress distributions and a universal elastic anisotropy index proposed recently is found and explained through a simple model. For macroscopic strain larger than the yield strain, the evolution of standard deviations with strain is rationalized by accounting only for the macroscopic elastic strain and the standard deviation of Taylor factor. These numerical results associated with physically-based simple models allow to estimate easily intergranular normal stress concentrations, constituting a tool for classifying polycrystalline aggregates according to their potential susceptibility to IGSCC.

*Keywords:* grain boundaries (A), stress concentrations (A), crystal plasticity (B), polycrystalline material (B), finite elements (C)

---

## 1. Introduction

InterGranular Stress-Corrosion Cracking (IGSCC) is a material degradation mode that has been observed experimentally for a wide range of materials and applications, for example in austenitic stainless steels (Nishioaka et al., 2008; Le Millier et al., 2013; Stephenson and Was, 2014; Gupta et al., 2016) and zirconium alloys (Cox, 1970, 1990) used in nuclear power plant environment, nickel-based alloys (Van Rooyen, 1975; Shen and Shewmon, 1990; Panter et al., 2006; IAEA, 2011) of steam generators, high strength aluminium alloys used as structural materials in moist air or aqueous environment (Speidel, 1975; Burleigh, 1991), and ferritic steels used for pipelines in presence of carbon-dioxide (Wang and Atrens, 1996; Arafin and Szpunar, 2009). All these IGSCC examples correspond to the initiation and propagation of cracks at grain boundaries (King et al., 2008). Various physical mechanisms have been proposed to explain IGSCC (Burleigh, 1991) - *e.g.* active path dissolution (Parkins, 1980), slip-dissolution (Newman and Healey, 2007), hydrogen embrittlement

---

\*Corresponding author

*Email addresses:* samir.elshawish@ijs.si (S. El Shawish), jeremy.hure@cea.fr (J. Hure)

(Beachem, 1972), localized deformation (Bieler et al., 2009; McMurtrey et al., 2015) - that depend on the material, the corrosive environment and the local stress state. As such, evaluation of intergranular stresses is required in order to quantitatively predict IGSCC. In the recent years, experimental assessment of grain boundaries stresses has become available through High Resolution Electron Back Scatter Diffraction (HR EBSD) (Gardner et al., 2010; McMurtrey et al., 2015) or Laue microdiffraction (Larson et al., 2002; Guo et al., 2015) which remains up to now limited to rather small number of grain boundaries and therefore does not allow to get statistical information about intergranular stress distributions.

On the modelling side using Crystal Plasticity constitutive equations, efforts have been made to obtain local stresses in polycrystalline aggregates using Finite Element Method (CPFEM) (Barbe et al., 2001a,b; Sauzay, 2007) or FFT method (Lebensohn et al., 2012). CPFEM has been used in particular to get intergranular stresses (Diard et al., 2002, 2005; Kanjarla et al., 2010; Gonzalez et al., 2014; Hure et al., 2016) providing valuable information for IGSCC initiation, *i.e.* for uncracked material. Coupling CPFEM with cohesive zone modelling at grain boundaries allowed to simulate both initiation and propagation of intergranular cracks (Diard et al., 2002; Musienko and Cailletaud, 2009; Couvant et al., 2013; Simonovski and Cizelj, 2014). From an engineering point of view, prediction of IGSCC initiation and especially its dependence on applied macroscopic stress, is of uttermost importance as it can provide safe operating range. Diard *et al.* (Diard et al., 2002, 2005) provided the evaluation of intergranular normal stresses as a function of the angle between the grain boundary and loading direction, considering Hexagonal Close Packed (HCP) crystal plasticity and uniaxial tension. Similar approach was followed in (Gonzalez et al., 2014) for Face-Centered Cubic (FCC) crystal plasticity in uniaxial tension, leading to the increase (or decrease) of intergranular normal stresses - compared to isotropic case - due to elastic and/or plastic anisotropy. In (Hure et al., 2016), intergranular normal stress distributions were obtained for FCC material for a realistic polycrystalline aggregate (Simonovski and Cizelj, 2011) that give statistical information about intergranular stresses. However, to the authors' knowledge, no systematic CPFEM studies have been performed up to now to provide statistical distributions of normal intergranular stresses as a function of elastic and plastic anisotropy arising from the considered slip systems (HCP, FCC, BCC) and loading conditions (uniaxial or biaxial) on polycrystalline aggregates. Owing to the different materials on which IGSCC can be observed, such study appears to be a key ingredient towards IGSCC initiation modelling and is therefore the objective of this paper.

In the first part of the paper, finite element simulations are described, including crystal-scale constitutive equations and computations of intergranular stresses. In the second part, probability density functions (*pdf*) of normal intergranular stresses for a wide range of situations - cubic and hexagonal elasticity, (FCC, BCC, HCP) crystal plasticity, uniaxial and equibiaxial loading - are presented. Standard deviations are used to quantify the broadening of the *pdfs* due to elastic and/or plastic mismatches. Simple formulas are proposed to rationalize the main numerical observations. The results are finally discussed regarding their range of validity and towards establishing a tool for a quick and reliable estimation of material susceptibility to IGSCC initiation.

## 2. Methods

### 2.1. Assumptions

Grains in a polycrystalline aggregate are modeled as three-dimensional (3D) homogeneous continua of convex shape. Voronoi partitioning of the modelling space is used to define the topology of the grains. The average grain is therefore assumed isotropic in shape, *i.e.* not elongated in any direction. 3D Voronoi tessellation has been extensively used over the last decade (Barbe et al., 2001a,b; Diard et al., 2005) since it produces a random virtual microstructure that captures some of the features of real microstructures (Fan et al., 2004).

In single-phase polycrystals, the material properties are the same for all the grains that are defined simply by their crystallographic orientation. In this study, grain orientations are assumed to be fully random, thus providing zero texture to the aggregate.

Polycrystalline simulations are performed using finite element discretization of the grains. To investigate the mechanical response of the aggregate under uniaxial and equibiaxial loading conditions, anisotropic elasticity and crystal plasticity material properties are assigned to each grain. No constitutive modelling of the grain boundaries is considered. Slip is furthermore assumed to be the only mechanism for plastic deformation. For simplicity, all slip systems (within FCC, BCC and HCP crystal systems) are assigned the same shear flow law and hardening behavior.

## 2.2. Finite element simulations

### 2.2.1. Material constitutive equations

A single crystal is assumed to behave as an anisotropic continuum. Constitutive relations in linear elasticity are governed by the generalized Hooke's law

$$\sigma_{ij} = C_{ijkl}\epsilon_{kl} \quad (1)$$

where  $\sigma_{ij}$  and  $\epsilon_{ij}$  are, respectively, the second-order stress and (elastic) strain tensors and  $C_{ijkl}$  the fourth-order stiffness tensor ( $i, j, k, l = 1 \dots 3$ ). Table 1 lists the elastic constants (in Voigt notation) used most often in this study.

	$C_{11}$ (GPa)	$C_{12}$ (GPa)	$C_{13}$ (GPa)	$C_{33}$ (GPa)	$C_{44}$ (GPa)
Al	107.3	60.9	60.9	107.3	28.3
Fe $\gamma$	197.5	125.0	125.0	197.5	122.0
Fe $\alpha$	231.4	134.7	134.7	231.4	116.4
Na	6.15	4.96	4.96	6.15	5.92
Zn	161.0	34.2	50.1	61.0	38.3

Table 1. Elastic constants of cubic (Al, Fe  $\gamma$ , Fe  $\alpha$ , Na) and hexagonal (Zn) single crystals taken from (Sauzay, 2007; Bower, 2010).

The plastic behavior of single crystal is described within crystal plasticity theory where plastic deformation is governed by slip alone. Crystal systems with associated slip systems used in this study are listed in Table 2. Deformations by other mechanisms such as diffusion, twinning or grain boundary sliding are not taken into account.

Crystal system	Slip plane $n$ / direction $s$			Number of slip systems
FCC	{111} <110>	-	-	12
BCC	{123} <111>	{112} <111>	{110} <111>	48
HCP1	{11 $\bar{2}$ 2} <11 $\bar{2}$ $\bar{3}$ >	-	-	6
HCP2	{0001} <1 $\bar{2}$ 10>	{11 $\bar{2}$ 2} <11 $\bar{2}$ $\bar{3}$ >	{10 $\bar{1}$ 0} <1 $\bar{2}$ 10>	12

Table 2. Crystal systems and associated slip systems (as, e.g., in (Mbiakop et al., 2015)).

The shear flow is modeled by visco-plastic behavior (Cailletaud, 1991; Hoc and Forest, 2001)

$$\dot{\gamma}^\alpha = \left\langle \frac{|\tau^\alpha| - \tau_c^\alpha}{K_0} \right\rangle^n \text{sign}(\tau^\alpha) \quad \text{with} \quad \langle x \rangle = \begin{cases} x & ; x > 0 \\ 0 & ; x \leq 0 \end{cases} \quad (2)$$

where  $\gamma^\alpha$  is the shear strain in slip system  $\alpha$  and  $\tau^\alpha$  and  $\tau_c^\alpha$  are, respectively, the resolved shear stress and critical resolved shear stress. Parameters  $K_0$  and  $n$  regulate the viscosity of the shear flow. Here,  $K_0 = 10$  MPa and  $n = 15$  have been considered, leading to almost negligible strain rate dependency on stresses for all simulations presented hereafter. This corresponds to the rate-independent limit of visco-plastic behavior modeled by Eq. (2).

To account for hardening, the critical resolved shear stress is additively decomposed into

$$\tau_c^\alpha = \tau_0 + H\Gamma \quad \text{with} \quad \Gamma = \sum_\alpha \int |\dot{\gamma}^\alpha| dt \quad (3)$$

where  $\tau_0$  denotes the initial critical resolved shear stress assumed to be the same for all slip systems and  $H \geq 0$  is the amplitude of linear Taylor hardening. An arbitrary value of  $\tau_0 = 100$  MPa is taken and discussed in Sec. 3. The purpose of using such a simple hardening behavior is to demonstrate the effects of finite hardening ( $H > 0$ ) in comparison to quasi-ideal plasticity ( $H = 0$ ). In Sec. 4 further investigation towards more realistic hardening behavior is considered. Similarly, the assumption of uniform critical resolved shear stress (CRSS) for HCP crystal systems listed in Table 2 is not intended to be realistic, but rather to investigate the effects of higher plastic anisotropy compared to FCC and BCC. A discussion about the effect of non-uniform CRSS is given in Sec. 4.

The constitutive law was implemented into two numerical codes – Abaqus (Simulia, 2016) and Cast3M (CEA, 2015) – to assess the influences of different integration methods on the robustness of results. In both implementations large deformation theory was accounted for by the usual multiplicative decomposition of the deformation gradient. The Abaqus implementation was accomplished through a UMAT subroutine following the implementation of Huang (Huang, 1991), where slight modifications were needed to accommodate the shear flow law of Eq. (2). In Cast3M the constitutive equations were generated by the MFront code generator (Helfer et al., 2015). Both implementations have been shown to give equivalent results. Details about numerical implementations can be found elsewhere (Hure et al., 2016).

### 2.2.2. Polycrystalline aggregates

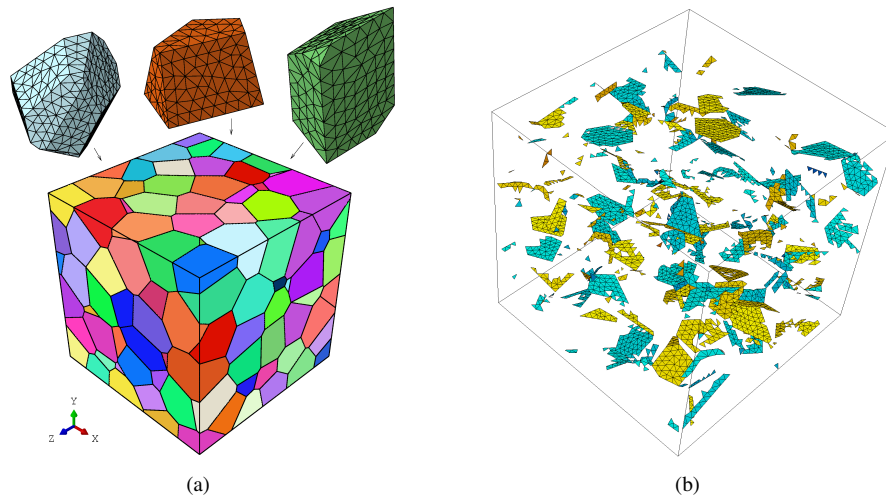


Figure 1. (a) Voronoi aggregate model with 200 grains with corresponding mesh density indicated on the three grains. (b) Set of intergranular elements for which normal stresses are larger than macroscopic stress  $\Sigma$  (obtained considering cubic elasticity of Fe  $\gamma$  for uniaxial tensile loading in y direction). Colors correspond to different grain boundary orientations.

Finite element models of polycrystalline aggregates were built from Voronoi tessellations made of 100 to 1000 grains and composed of 130k to 1400k tetrahedral quadratic elements (C3D10 in Abaqus). Voronoi tessellations were obtained using non-zero repulsion distance between the seeds to avoid tiny edges which were shown in (Gonzalez et al., 2014) to be the source of unphysically large variability of intergranular stresses. Random initial crystallographic orientations were assigned to the grains to introduce zero texture. Figure 1(a) shows the Voronoi aggregate with 200 grains used in this study. Except in Sec. 4.1 where the influence of using different Voronoi aggregates is studied in more detail, all results presented hereafter have been obtained on this aggregate with one set of random crystallographic orientations. The variability regarding intergranular stresses due to different sets of random crystallographic orientations and/or aggregates through the presence of small boundaries were evaluated in (Gonzalez et al., 2014) for a given set of material properties. On the contrary, the purpose of this study is to quantify separately the effects of material properties, therefore requiring the same aggregate/crystallographic orientations for all the simulations.

In the case of uniaxial loading, incremental tensile displacement is applied along X axis to all the nodes on front surface, while keeping the nodes on back surface constrained to have zero axial displacement. In the case of equibiaxial loading, same displacements and constraints are applied along the additional Y axis. In both cases nodes on the lateral (free) surfaces are not constrained so as to study the free surface effects, relevant for IGSCC. Such boundary conditions, approximating periodic boundary conditions by keeping the opposite surfaces (of normal X and Y) flat, have been shown to lead to local disturbances of the stress field. However, this artifact was checked to have a negligible effect on the stress distributions shown hereafter (see Appendix A). Moreover, especially in the cases where no grain-scale hardening is considered, local necking is expected to appear leading to a strain gradient along the loading direction that complicates the interpretation of the results. Thus, small applied macroscopic strains are considered in this study, which are relevant for IGSCC initiation phenomenon. In addition, the deformed aggregates are checked at the end of each simulation in order to assess the potential occurrence of local necking. The applied nominal strain in

the uniaxial and equibiaxial loading is respectively  $\Delta x/x_0 = 0.05$  and  $\Delta x/x_0 = \Delta y/y_0 = 0.05$ , while the associated strain rate is set to  $10^{-3} \text{ s}^{-1}$ . The macroscopic Cauchy stress tensor  $\Sigma$  is computed by dividing the resulting force on the boundaries where loading is applied by the *actual* section, leading to  $\Sigma \approx \Sigma e_X \otimes e_X$  for uniaxial loading (and  $\Sigma \approx \Sigma(e_X \otimes e_X + e_Y \otimes e_Y)$  for equibiaxial loading) as a result of the boundary conditions and the absence of crystallographic texture. The scalar value  $\Sigma$  is used in the following as a measure of stress amplitude. All stress distributions shown in Sec. 3, once normalized by the macroscopic stress  $\Sigma$ , were checked to be practically independent of the number of grains and mesh density.

### 2.2.3. Intergranular stress computations

Simulations performed on polycrystalline aggregates allow to obtain probability density functions (thereafter noted *pdf*) of normal stresses ( $\sigma_m$ ) between adjacent grains as a function of elastic anisotropy, plastic anisotropy, applied macroscopic strain and loading conditions (uniaxial or equibiaxial). As brittle cracking of grain boundaries is dependent on local stress state, these *pdfs* are believed to be a key ingredient towards IGSCC modelling.

For each pair of tetrahedral elements defining a boundary between two grains<sup>1</sup>, the Cauchy stress tensors  $\sigma$  at the closest Gauss points<sup>2</sup> near the boundary are obtained. These are then converted to normal stresses,  $\sigma_m = n \cdot \sigma \cdot n$ , knowing the normal  $n$  of the grain boundary facet. The projected stresses computed at various Gauss points are then averaged (with equal weights) to yield one single value for the normal stress per element pair. As elements of different sizes are used in the mesh, the occurrence of  $\sigma_m$  in the computation of *pdf* is weighted by the surface of the grain boundary facet on which it was obtained. One may note, however, that such weighting has only small effect on the results.

The method introduced here to obtain intergranular stresses differs slightly from those used in (Diard et al., 2002) and (Gonzalez et al., 2014). In the former, additional Gauss points were considered in elements close to grain boundaries, while cohesive elements were added to the model in the latter to obtain stresses exactly at grain boundaries. It is also known (El Shawish et al., 2013) that, in addition to large scatter, the accuracy of cohesive elements (in Abaqus) is questionable, especially when the grains are plastically strained. The rather simple method used in this study has, however, shown (see (Hure et al., 2016)) to be accurate enough to provide converged global shapes of the distributions upon refining the mesh. Moreover, the robustness of the method used here is assessed in more details in Appendix B where it is shown that using special tetrahedral elements (C3D10I in Abaqus) with Gauss points located at the nodes (therefore exactly on the grain boundary) leads to similar results regarding the moments (mean and standard deviation) of *pdfs*. Same conclusion is also obtained by averaging intergranular normal stresses on grain facets composed of numerous triangular elements (see Fig. 1 b).

It is important to note that in absence of material anisotropy the *pdf* of normal stress behaves as  $1/2 \sqrt{\sigma_m/\Sigma}$  for uniaxial and as  $1/2 \sqrt{1 - \sigma_m/\Sigma}$  for equibiaxial loading conditions, where  $\sigma_m$  is trivially bounded by  $\Sigma$  (see Appendix C for derivation). However, the upper bound can be easily exceeded when the mismatch effects between adjacent grains become important. Figure 1(b) demonstrates such an example where only those intergranular elements are shown for which normal stresses are larger than macroscopic stress,  $\sigma_m > \Sigma$ , assuming anisotropic elasticity of the grains and uniaxial tensile loading conditions. These elements are expected to either have small angle between their grain boundary facet normal  $n$  and loading

<sup>1</sup> Tetrahedral element can touch grain boundary either with its facet, edge or node. In this study, only pairs of tetrahedra are considered which share common grain boundary facet. In this case the associated facet area and normal are well defined for further calculation of *pdf*.

<sup>2</sup> Tetrahedral element C3D10 has four Gauss points placed close to the element corners. The three Gauss points belonging to the corners in contact with the grain boundary were selected as closest Gauss points.

direction and/or be at the boundary between two grains having strong elastic/plastic mismatches and/or be positioned close to geometric discontinuities (edges or triple points) where stress concentrations may be present.

### 3. Intergranular stress distributions

In this section, intergranular normal stress distributions obtained through finite element simulations on Voronoi aggregates are described, considering crystal elasticity and/or plasticity (with different slip systems), for both uniaxial and equibiaxial loading conditions.

#### 3.1. Crystal elasticity

Only crystal elasticity is considered in this part, which corresponds to the case of polycrystalline aggregates loaded below their macroscopic yield stress.

To follow the same nomenclature as used later for crystal plasticity, cubic symmetry is specified as FCC or BCC and hexagonal symmetry as HCP.

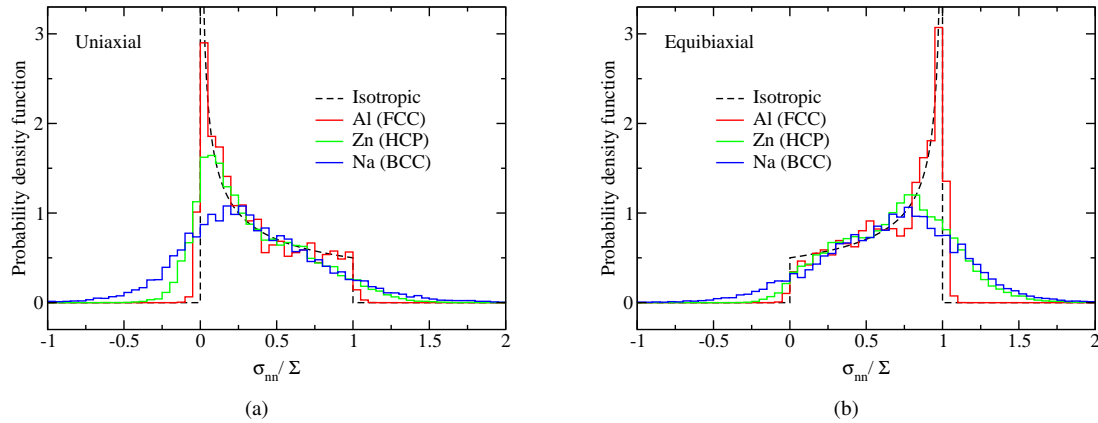


Figure 2. Probability density functions of normalized intergranular normal stress calculated with Voronoi finite element simulations assuming crystal elasticity and (a) uniaxial and (b) equibiaxial loading conditions.

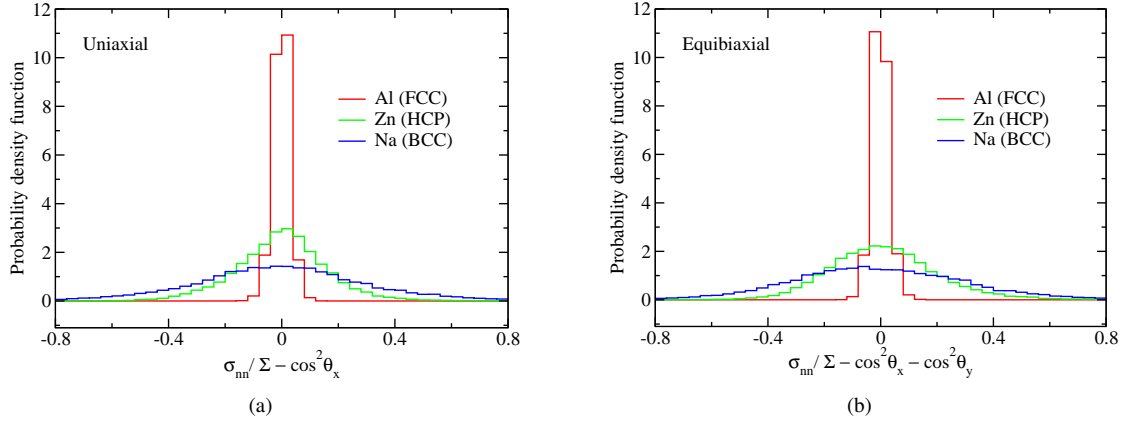


Figure 3. Probability density functions of normalized intergranular normal stress reduced by its isotropic contribution calculated with Voronoi finite element simulations assuming crystal elasticity and (a) uniaxial and (b) equibiaxial loading conditions.  $\theta_x$  and  $\theta_y$  are the angles between grain boundary normal and loading directions along X and Y axes, respectively.

As mentioned in the previous section, in the absence of material anisotropy intergranular stresses  $\sigma_{nn}$  are bounded by  $\Sigma$ , where  $\Sigma$  is the macroscopic stress. However, the upper bound can be easily exceeded when the mismatch effects between the adjacent grains become important, *i.e.* when material anisotropy is finite. Figures 2(a) and 2(b) show the calculated intergranular normal stress distributions obtained through finite element simulations on Voronoi aggregate for, respectively, uniaxial and equibiaxial loading conditions, on three different materials: Al with FCC, Na with BCC and Zn with HCP lattice symmetry.

The three materials were chosen to show the evolution of the *pdf* shape from isotropic-like (Al case) through bimodal-like (Zn case) towards normal-like shape (Na case). In the three cases, the mean values remain close to the theoretical value of  $1/3$  in the absence of material anisotropy.

It seems reasonable to expect that broadening of the distributions arises due to stronger mismatch effects between the grains which may be characterized by elastic anisotropy of the grains. Being almost isotropic at the crystal scale, polycrystalline Al has distributions in close agreement with the assumption of uniform stress, as mismatch effects between the grains are small (Figs. 2(a) and 2(b)). On the contrary, one of the most anisotropic metallic materials with BCC symmetry (Na) or HCP symmetry (Zn) show considerably wider distributions where significant probabilities are associated with intergranular normal stress larger than macroscopic stress.

The influence of anisotropy is analysed further in Figs. 3(a) and 3(b) where *pdfs* of normalized intergranular normal stress reduced by its isotropic counterpart,  $(\sigma_{nn} - \sigma_{nn}^{iso})/\Sigma$ , are presented with  $\sigma_{nn}^{iso} = \Sigma \cos^2 \theta_x$  for uniaxial tensile and  $\sigma_{nn}^{iso} = \Sigma(\cos^2 \theta_x + \cos^2 \theta_y)$  for equibiaxial loading conditions, respectively. Here,  $\theta_x$  and  $\theta_y$  are the angles between grain boundary normal and loading directions along X and Y axes, respectively. The obtained normal-like distributions for all the cases show the corresponding distribution widths growing with the increasing mismatch effects, in agreement with the observations in Figs. 2(a) and 2(b). It thus seems natural to use the first two statistical moments - mean and variance (or standard deviation) - to describe the distributions of  $(\sigma_{nn} - \sigma_{nn}^{iso})/\Sigma$ . The mean value is observed to be close to zero (which is consistent with the constant mean value of  $\sigma_{nn}/\Sigma$ ), while the standard deviation (hereafter denoted by  $s$ ) depends on the elastic anisotropy of the grains.

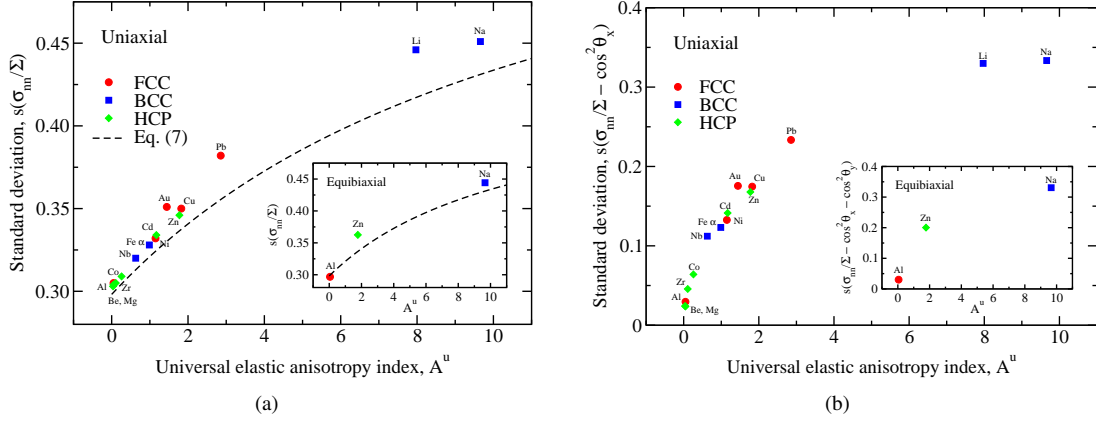


Figure 4. Comparison of universal elastic anisotropy index  $A^u$  with (a) standard deviation of normalized intergranular normal stress for uniaxial tensile loading (inset: equibiaxial loading) and (b) standard deviation of normalized intergranular normal stress reduced by its isotropic contribution for uniaxial tensile loading (inset: equibiaxial loading). Crystal elasticity was considered in Voronoi finite element simulations to calculate standard deviations.  $A^u$  was calculated for infinite random polycrystal using analytic formulae given in Appendix D. Dashed line in (a) represents a relationship given in Eq. (7).

The elastic anisotropy can be characterized conveniently by the universal elastic anisotropy index  $A^u$  introduced in (Ranganathan and Ostaja-Starzewski, 2008) as

$$A^u = 5 \frac{G^V}{G^R} + \frac{K^V}{K^R} - 6 \quad (4)$$

where  $G$  and  $K$  denote shear and bulk moduli, and superscripts  $V$  and  $R$  represent the Voigt and Reuss estimates, respectively. Unlike *e.g.* Zener index (Zener, 1948) for cubic materials,  $A^u$  can be applied to any lattice symmetry to describe the elastic anisotropy ( $A^u = 0$  corresponds to elastic isotropy). Roughly speaking, this universal anisotropy index is proportional to the ratio of Voigt (Voigt, 1928) to Reuss (Reuss, 1929) bounds of the elastic modulus for an aggregate with no crystallographic texture.

In this study, index  $A^u$  was calculated for several most common cubic (FCC and BCC) and hexagonal (HCP) metallic materials assuming infinitely large polycrystals with random grain orientations (see Appendix D for more detail). For each material the calculated  $A^u$  is shown in Fig. 4 along with the corresponding standard deviation  $s$  of  $\sigma_{nn}/\Sigma$  (in Fig. 4(a)) and  $(\sigma_{nn} - \sigma_{nn}^{iso})/\Sigma$  (in Fig. 4(b)), both calculated on a finite Voronoi aggregate under uniaxial and equibiaxial loading conditions. A clear monotonic relationship is observed in Figs. 4(a) and (b) for all considered materials (FCC, BCC and HCP), which suggests that the elastic anisotropy index  $A^u$  is able to faithfully describe standard deviation of normalized intergranular normal stresses. Since both variants,  $s(\sigma_{nn}/\Sigma)$  and  $s((\sigma_{nn} - \sigma_{nn}^{iso})/\Sigma)$ , seem to correlate equally well with the universal elastic anisotropy index  $A^u$ , the former one is selected for further investigation as *pdf* of  $\sigma_{nn}/\Sigma$  allows to associate the tails of distributions directly with larger intergranular stresses and with their probability of appearance in the model. In this respect, for example, it is easy to verify in Fig. 2 that equibiaxial loading condition, in comparison to uniaxial tensile loading, produces higher *pdf* tails on a tensile (right) side, which may indicate, statistically, more likely initiation of IGSCC. This observation, on contrary, could not be deduced directly from the *pdfs* of  $(\sigma_{nn} - \sigma_{nn}^{iso})/\Sigma$  in Fig. 3.

The evolution of the standard deviation of normalized normal intergranular stresses with the universal anisotropy index  $A^u$  can be understood as follows. Considering a polycrystalline aggregate in uniaxial (or equibiaxial) tension with macroscopic strain  $E$ , the maximum (intergranular normal) stress magnitude in the

aggregate can be estimated using Voigt's upper bound,  $\sigma_{nn}^{max.} \approx Y_{Voigt} E$ . The minimal value is assumed to be close to zero  $\sigma_{nn}^{min.} \approx 0$ , which corresponds to grain boundaries parallel to the loading direction. The macroscopic stress of the aggregate is equal to  $\Sigma = Y E$ , where  $Y$  is the effective Young's modulus. For most aggregates,  $Y$  can be fairly well approximated as the arithmetic mean of Voigt and Reuss estimations of Young's modulus,  $Y \approx (Y_{Voigt} + Y_{Reuss})/2$ , as proposed by Hill. As the standard deviation of  $\sigma_{nn}/\Sigma$  scales with the measurement range,

$$s\left(\frac{\sigma_{nn}}{\Sigma}\right) \sim \frac{\sigma_{nn}^{max.} - \sigma_{nn}^{min.}}{\Sigma} \approx \frac{4}{3\sqrt{5}} \frac{1}{1 + Y_{Reuss}/Y_{Voigt}} \quad (5)$$

where the prefactor  $4/3\sqrt{5}$  is used to recover the exact result for isotropic crystals. Moreover, neglecting the differences between Voigt and Reuss bounds of Poisson's ratio, the universal anisotropy index can be approximated as

$$A^u \approx 6(Y_{Voigt}/Y_{Reuss} - 1). \quad (6)$$

Equation (6) is shown in Appendix D to be a good approximation (with error smaller than  $\sim 15\%$ ) of the universal anisotropy index. Combining Eq. (6) with Eq. (5) leads to the estimation of the standard deviation as a function of the universal anisotropy index  $A^u$

$$s\left(\frac{\sigma_{nn}}{\Sigma}\right) \approx \frac{4}{3\sqrt{5}} \frac{A^u + 6}{A^u + 12}. \quad (7)$$

Equation (7) is compared to the numerical results in Fig. 4a. Despite simplified assumptions used in the derivation, Eq. (7) is able to capture the evolution of the standard deviation of the normalized intergranular normal stresses with the universal anisotropy index  $A^u$ .

The results of this section concerning intergranular normal stresses  $\sigma_{nn}$  in an elastic untextured polycrystal can be summarized into the following few statements:

- Independently of the anisotropy of the single crystal, the mean value of  $\sigma_{nn}/\Sigma$  is equal to  $1/3$  and  $2/3$  for uniaxial and equibiaxial loading conditions, respectively.
- Standard deviation of  $\sigma_{nn}/\Sigma$  increases with the anisotropy of the single crystal: a clear monotonic relationship between the standard deviation and the universal elastic anisotropy index  $A^u$  proposed by (Ranganathan and Ostaja-Starzewski, 2008) is observed, and a simple model (Eq. (7)) is proposed to explain and describe this relationship.
- The universal anisotropy index  $A^u$  can thus be used through Eq. (7) to assess the potential susceptibility of a polycrystalline aggregate to IGSCC.
- Equibiaxial loading condition is shown to be more damaging with respect to the initiation of IGSCC than uniaxial tensile loading.

The results presented in this section regarding the mean and standard deviation of normalized normal intergranular stresses are valid for untextured polycrystalline aggregates loaded below their macroscopic yield stress.

The influence of plastic effects on the evolution of  $s(\sigma_{nn}/\Sigma)$  at strains close or well above the yield strain is going to be studied in the next section.

### 3.2. Crystal elasticity and plasticity

In this part, both crystal elasticity and plasticity are accounted for in numerical simulations of polycrystalline aggregate, and probability density functions of intergranular normal stress are shown as a function of total strain up to 5%, *i.e.* well above the yield strain. The focus is set on studying the evolution of  $s(\sigma_{nn}/\Sigma)$  with applied strain to identify main elastic and plastic contributors to the broadening of the *pdf*.

#### 3.2.1. Typical observations

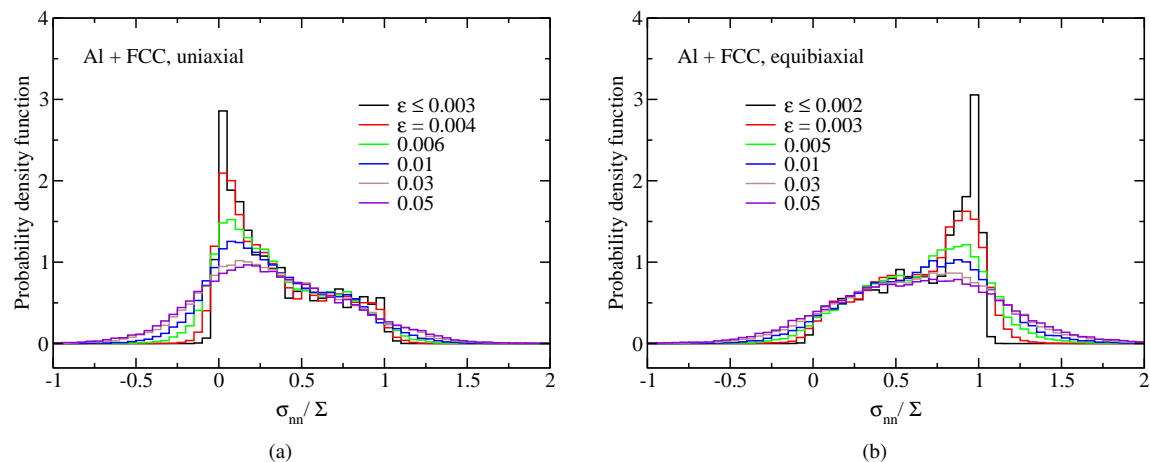


Figure 5. Probability density functions of normalized intergranular normal stress calculated with Voronoi finite element simulations at various strains assuming crystal elasticity and ideal ( $H = 0$ ) plasticity for Al and FCC under (a) uniaxial and (b) equibiaxial loading conditions.

Figure 5 shows the evolution of *pdf* with strain for two loadings (tensile and equibiaxial) considering Al elasticity and FCC slip systems (and no hardening). For total strain below yield strain, distributions are the same as the ones presented in Sec. 3.1. For larger strains, a significant broadening of *pdf* is observed, with a shape change from iso-like (Al has small elastic anisotropy) through bi-modal (moderate strain) towards normal-like shape (large strain). The evolution of pdf shape with strain is very similar to the one observed in Fig. 2 for different materials. Therefore, broadening of pdf with strain, also observed for other materials (with different crystal elasticity parameters and slip systems) as shown in the following sections, is assumed to be the result of the increase of (plastic) anisotropy of the grains. Additional simulations (not shown here) performed in the small strain limit (to avoid any texture evolution) or for different viscosity parameters used in the constitutive equations lead to similar results, thus confirming that the broadening is only due the local grain-grain interactions. A similar broadening of intergranular stress distributions with strain was reported in previous studies, *e.g.*, (Diard et al., 2002; Gonzalez et al., 2014).

For all simulations, independently of crystal elasticity parameters and slip systems considered, the mean values of normalized intergranular normal stresses remain approximately constant<sup>3</sup> at  $\sim 1/3$  and  $\sim 2/3$  for uniaxial and equibiaxial loading conditions, respectively. As in Sec. 3.1, the broadening of distributions is quantified through the evolution of standard deviations in the following sections.

<sup>3</sup> With larger strain the grains become elongated and may develop small texture. Both effects may change the mean value of *pdf*.

### 3.2.2. Without hardening

The evolution of standard deviation of normalized intergranular stress as a function of elastic properties is shown in Fig. 6, considering FCC slips systems with no hardening. For low applied total strain, constant values are obtained in quantitative agreement with purely elastic simulations presented in Sec. 3.1, for both uniaxial and equibiaxial loading conditions. For large applied strain, standard deviations are found to increase with strain. For all cases considered, the value of strain at which  $s(\sigma_{nm}/\Sigma)$  starts to deviate from elastic value corresponds to the onset of plasticity (macroscopic yield strain  $\epsilon_y$ ) observed in tensile curves (inset Fig. 6), in agreement with what was reported in (Gonzalez et al., 2014). This defines an elastic regime where only elastic properties influence intergranular normal stress distributions and an elasto-plastic regime where both elastic properties and slip systems dictate the evolution of  $s(\sigma_{nm}/\Sigma)$ .

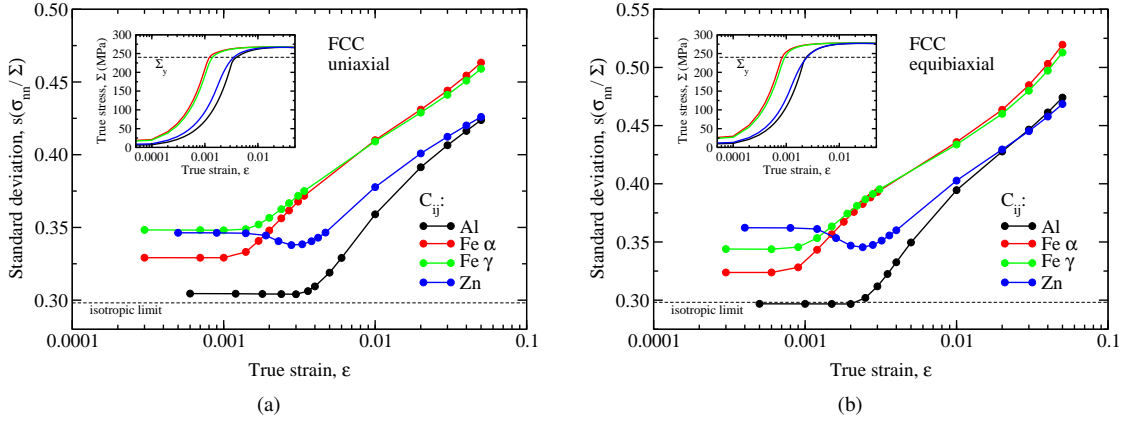


Figure 6. Standard deviation of normalized intergranular normal stress (inset: macroscopic tensile stress) as a function of applied strain calculated with Voronoi finite element simulations assuming crystal elasticity and ideal ( $H = 0$ ) plasticity for various materials and FCC under (a) uniaxial and (b) equibiaxial loading conditions.

As yield strain  $\epsilon_y$  is a result of both elastic and plastic properties, therefore being different for simulations shown in Fig. 6, a natural rescaling is to consider  $\epsilon \rightarrow \epsilon/\epsilon_y$ . With this rescaling, a universal curve is observed in the plastic regime, as shown in Fig. 7, where both elastic properties and initial critical resolved shear stress have been changed, for both uniaxial and equibiaxial loading conditions. Thus, the evolution of  $s(\sigma_{nm}/\Sigma)$  with rescaled strain  $\epsilon/\epsilon_y$  is found to be practically independent of elastic properties in plastic regime ( $\epsilon \gg \epsilon_y$ ), in accordance with the results presented in (Gonzalez et al., 2014) for specific conditions.

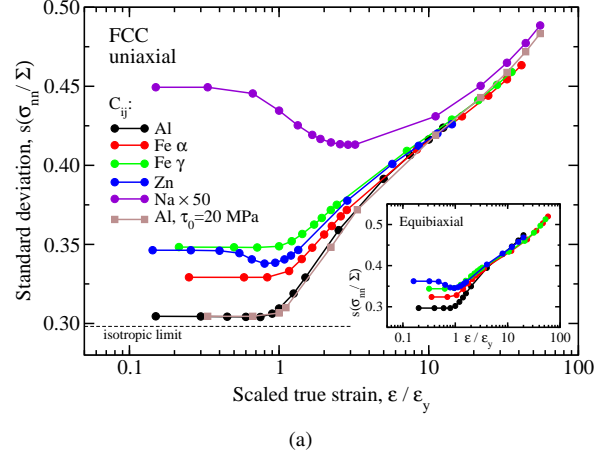


Figure 7. Standard deviation of normalized intergranular normal stress as a function of applied strain rescaled by yield strain calculated with Voronoi finite element simulations assuming crystal elasticity and ideal ( $H = 0$ ) plasticity for various materials and FCC under uniaxial (inset: equibiaxial) loading conditions. Note that elastic constants of Na were multiplied by 50 to reduce  $\epsilon_y$  (but keeping the same elastic anisotropy). All simulations were performed with  $\tau_0 = 100$  MPa except the last one for Al and  $\tau_0 = 20$  MPa.

The universal behavior observed in Fig. 7 for  $s(\sigma_{nm}/\Sigma)$  as a function of rescaled strain  $\epsilon/\epsilon_y$  can be understood using the following reasoning. Let us consider two materials  $I$  and  $II$  such that

$$C_{ijkl}^{II} = k_C C_{ijkl}^I, \quad \tau_0^{II} = k_\tau \tau_0^I \quad (8)$$

where  $k_C, k_\tau$  are constant factors, and with both materials having the same set of slip systems defined through Schmid tensor  $\mu_{kl}$ . For arbitrary location  $\mathbf{r}$  and time  $t$ , the stress and strain components obey Eqs. (1), (2) and (3) combined into (omitting  $\mathbf{r}$  and  $t$  hereafter for clarity)

$$\dot{\sigma}_{ij} = C_{ijkl} \left( \dot{\epsilon}_{kl} - \sum_{\alpha} \left\langle \frac{|\sigma_{pq} \mu_{pq}^{\alpha}| - \tau_0}{K_0} \right\rangle^n \text{sign}(\sigma_{pq} \mu_{pq}^{\alpha}) \mu_{kl}^{\alpha} \right) \quad (9)$$

where same definitions for elastic ( $C_{ijkl}$  for  $i, j, k, l = 1 \dots 3$ ) and plastic ( $\tau_0, K_0, n$ ) material parameters are used as in Sec. 2.2.1. At a given time  $t$ , assuming the following rescaling for the stress and strain components and viscosity parameters,

$$\sigma_{ij}^{II} = k_\tau \sigma_{ij}^I, \quad \epsilon_{ij}^{II} = \frac{k_\tau}{k_C} \epsilon_{ij}^I, \quad K_0^{II} = k_\tau \left( \frac{k_\tau}{k_C} \right)^{-1/n} K_0^I, \quad n^{II} = n^I, \quad (10)$$

along with Eq. (9) leads to  $\dot{\sigma}_{ij}^{II} = k_\tau \dot{\sigma}_{ij}^I$ , indicating that Eqs. (10) hold in fact at any time. Equation (10<sub>2</sub>) can be rewritten as  $\epsilon_{ij}^{II}/\epsilon_y^{II} = \epsilon_{ij}^I/\epsilon_y^I$ , suggesting to write the standard deviation of normalized intergranular normal stress as a function of applied strain rescaled by yield strain for materials satisfying Eqs. (8). The condition set by Eq. (10<sub>3</sub>) is not met in the simulations where  $K_0$  is kept constant. However, this parameter has negligible influence on the results in the rate-independent limit  $K_0 \dot{\epsilon}_0^{1/n} \ll \tau_0$ . Moreover, despite the fact that the argument given here suggests the rescaling applies only for a specific class of materials (set by Eqs. (8)), Fig. 7 shows that it can be applied in a broader context that remains to be precisely defined theoretically.

For small values of applied strain,  $\epsilon \ll \epsilon_y$ , Eq. (9) reduces to Hooke's law as  $|\sigma_{pq}\mu_{pq}^\alpha| \leq \tau_0$ . In this regime, the standard deviation of normalized intergranular stress is constant and in quantitative agreement with the one described in Sec. 3.1. For large values of applied strain,  $\epsilon \gg \epsilon_y$ , all grains are assumed to deform plastically and Eq. (9) reduces to

$$\dot{\epsilon}_{kl} \approx \sum_{\alpha} \left\langle \frac{|\sigma_{pq}\mu_{pq}^\alpha| - \tau_0}{K_0} \right\rangle^n \text{sign}(\sigma_{pq}\mu_{pq}^\alpha) \mu_{kl}^\alpha. \quad (11)$$

Continuity requirement of normal stress and strain components at a grain boundary associated with Eq. (11) is believed to lead to the increase of intergranular normal stress with strain. Note that Eq. (11) does not involve explicitly the elastic properties which appears to be consistent with the numerical observation that the evolution of  $s(\sigma_{nn}/\Sigma)$  as a function of  $\epsilon/\epsilon_y$  does not depend on elastic properties.

The transition between both regimes is observed to depend on the elastic parameters, as already reported in Lebensohn et al. (2012), and can be qualitatively understood considering the strain-dependent anisotropy of grains. At the onset of macroscopic plasticity,  $\epsilon \sim \epsilon_y$ , an increase of  $s(\sigma_{nn}/\Sigma)$  can be explained through the gradual activation of slip systems (where regions with more activated slip systems provide smaller plastic anisotropy), thus to plastic slip that can only occur along few particular slip directions (keeping the deformation in all other directions elastic). On the contrary, a decrease of  $s(\sigma_{nn}/\Sigma)$  observed in Fig. 7 for Na and Zn can be understood to appear due to specific alignment of stiffness and Schmid tensors which enables slip activation along the hardest grain direction, thus reducing maximum stress and therefore stress fluctuations.

For a given set of elastic properties (Al from Tab. 1), the evolution of intergranular normal stress standard deviation with strain is assessed in Fig. 8 for different sets of slips systems. In the plastic regime, a log-like behavior is observed for all simulations. However, the typical slope of the line (using lin-log type of plotting) depends on the set of slip systems considered: the highest slope is found for HCP1 and the lowest for HCP2, while FCC and BCC lead to similar evolutions. Same qualitative behavior is observed for uniaxial and equibiaxial loading conditions.

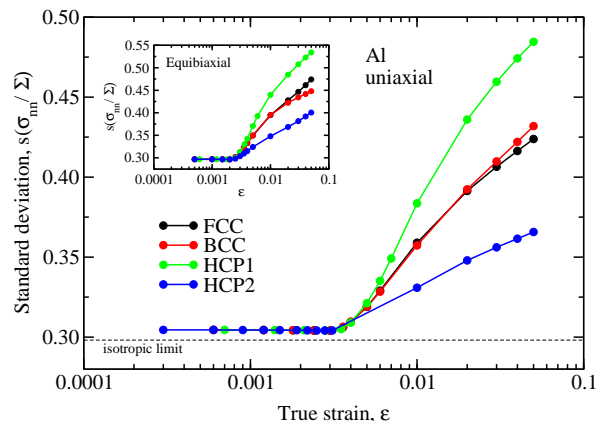


Figure 8. Standard deviation of normalized intergranular normal stress calculated with Voronoi finite element simulations as a function of applied strain assuming crystal elasticity and ideal ( $H = 0$ ) plasticity for Al and various slip systems under uniaxial (inset: equibiaxial) loading conditions.

### 3.2.3. With hardening

Results presented in Sec. 3.2.2 regarding the effects of elastic and plastic properties on the evolution of standard deviations of intergranular normal stress distributions correspond to the case of zero hardening

( $H = 0$  in Eq. 3). For a given set of elastic property and slip system, the effect of (Taylor-)hardening on  $s(\sigma_{mn}/\Sigma)$  in plastic regime is evaluated in Fig. 9 for both uniaxial and equibiaxial loading conditions. For a given strain value, the larger the hardening modulus, the lower the standard deviation  $s(\sigma_{mn}/\Sigma)$ . The same behavior is observed for other combinations of elastic properties and slip systems (not shown).

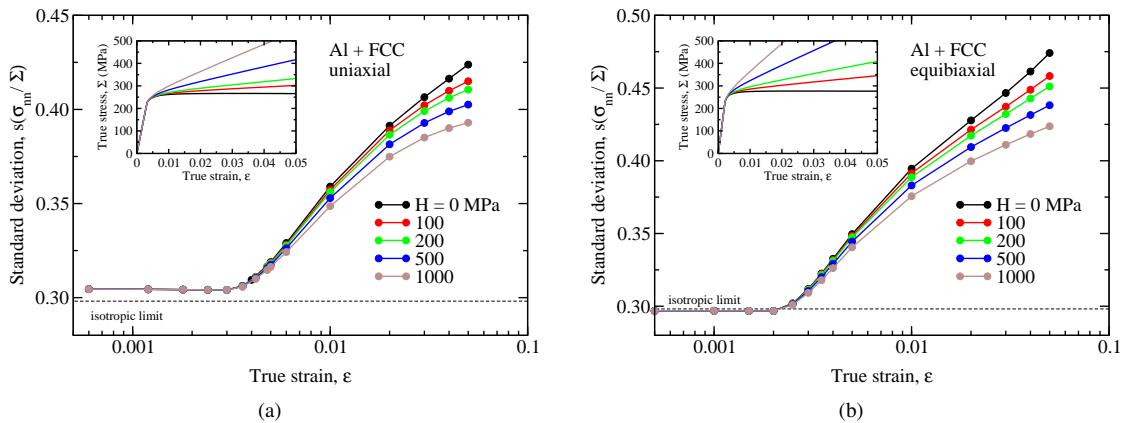


Figure 9. Standard deviation of normalized intergranular normal stress (inset: macroscopic tensile stress) as a function of applied strain calculated with Voronoi finite element simulations assuming crystal elasticity and plasticity for Al and FCC with various hardening strengths under (a) uniaxial and (b) equibiaxial loading conditions.

Hardening induces the evolution of critical resolved shear stress with macroscopic strain,  $\tau_c^\alpha(\epsilon) = \tau_0 + H\Gamma(\epsilon)$ , according to Eq. (3), which results in the evolution of macroscopic stress  $\Sigma(\epsilon)$ . For a given macroscopic strain  $\epsilon$ , an identical value of macroscopic stress can be achieved by considering a material with no hardening ( $H = 0$ ), but with appropriately larger constant critical resolved shear stress. Since in this way both materials would share several macroscopic quantities at a given strain (*e.g.*, macroscopic stress  $\Sigma(\epsilon)$ , macroscopic elastic strain  $\epsilon_{el}(\epsilon)$  and macroscopic plastic strain  $\epsilon_{pl}(\epsilon)$ ), we may assume that, at same strain and restricting to monotonic loading, they would become equivalent also with respect to standard deviation of intergranular normal stress distribution  $s(\sigma_{mn}/\Sigma)$ . This assumption leads to a natural extension of the rescaling used in Sec. 3.2.2, which is to consider  $\epsilon \rightarrow \epsilon/\epsilon_{el}$ . For  $H = 0$ ,  $\epsilon \rightarrow \epsilon/\epsilon_{el}$  would give the same result as shown in Fig. 7 for other materials. Such a rescaling allows to get a universal curve in the plastic regime as shown in Fig. 10.

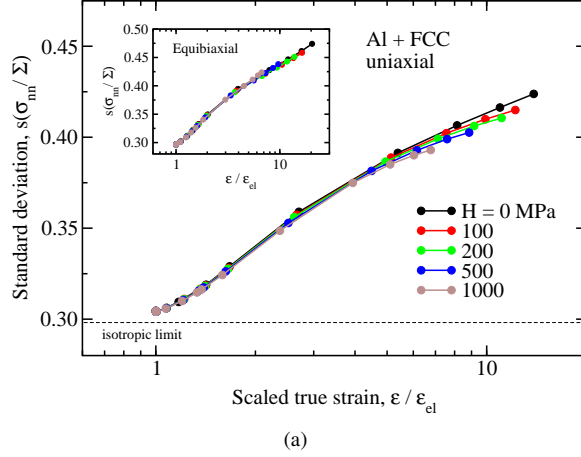


Figure 10. Standard deviation of normalized intergranular normal stress as a function of applied strain rescaled by elastic strain calculated with Voronoi finite element simulations assuming crystal elasticity and plasticity for Al and FCC with various hardening strengths under uniaxial (inset: equibiaxial) loading conditions.

As an intermediate conclusion, simulations performed on Voronoi aggregates with different elastic properties, sets of slip systems and (Taylor-)hardening have led to the following observations regarding standard deviation of normalized intergranular normal stress distributions  $s(\sigma_{nm}/\Sigma)$ :

- For strain values below macroscopic yield strain  $\epsilon < \epsilon_y$ ,  $s(\sigma_{nm}/\Sigma)$  is constant and depends solely on elastic properties (as described in Sec. 3.1).
- For strain values well above macroscopic yield strain  $\epsilon \gg \epsilon_y$ ,  $s(\sigma_{nm}/\Sigma)$  was found to follow a universal behavior when plotted as a function of rescaled strain  $\epsilon/\epsilon_{el}$ , where  $\epsilon_{el}$  is the macroscopic elastic strain.

The function  $\mathcal{F}$  that relates the standard deviation of intergranular normal stress to the normalized strain,  $s(\sigma_{nm}/\Sigma) = \mathcal{F}(\epsilon/\epsilon_{el})$ , depends on the set of slip systems considered, as shown in Fig. 8. The aim of the next section is to provide a simple model for predicting such behavior.

### 3.2.4. Combined effects – universal behavior

Figure 11a summarizes the evolution of  $s(\sigma_{nm}/\Sigma)$  in plastic regime with rescaled strain  $\epsilon/\epsilon_{el}$  in uniaxial loading conditions, for different elastic parameters, sets of slip systems and hardening modulus. As discussed previously, this evolution appears to depend practically only on the chosen slip system (independently of elastic properties and hardening strength) under the assumption of uniform critical resolved shear stress. In the plastic regime (*i.e.*, for  $3 \lesssim \epsilon/\epsilon_{el} \lesssim 10$ ), the evolution of  $s(\sigma_{nm}/\Sigma)$  can be well approximated by the following log-like equation

$$s(\sigma_{nm}/\Sigma) \approx s_{iso} + k \ln(2\epsilon/\epsilon_{el}) \quad (12)$$

with  $k$  parameter defining the strain-independent part of plastic anisotropy, and where  $s_{iso} = 2/3 \sqrt{5}$  is the standard deviation of  $s(\sigma_{nm}/\Sigma)$  in an aggregate with isotropic grains ( $k = 0$ ), corresponding to the case of an infinite number of slip systems (Tresca plasticity) or von Mises plasticity. In the latter case, it has been checked that  $s(\sigma_{nm}/\Sigma) = s_{iso}$ .

Moreover, Fig. 11(b) shows a very good linear correlation between  $k$  and standard deviation of Taylor factor,  $s(M)$ , (calculated in Appendix E)

$$s(\sigma_{nm}/\Sigma) \approx s_{iso} + 0.10s(M) \ln(2\epsilon/\epsilon_{el}) \quad (13)$$

for uniaxial loading conditions. A very similar behavior has been observed for equibiaxial loading conditions (not shown), however with a prefactor  $0.12s(M)$  identified in Eq. (13), where  $s(M)$  is the same as for uniaxial loading conditions. The proportionality of standard deviation of intergranular normal stress distribution can be understood as follows: using Taylor's homogeneous strain assumption in the aggregate (see Appendix E), the local (von Mises) stress can be written as  $\sigma \sim M\tau$  where  $M$  is Taylor factor and  $\tau$  the critical resolved shear stress. Similar relation holds also at the macroscopic scale:  $\Sigma \sim \langle M \rangle \tau$  where  $\langle M \rangle$  denotes average Taylor factor. Standard deviation of  $\sigma_{nm}/\Sigma$  therefore scales as standard deviation of Taylor factor, which is in accordance with results of the simulations.

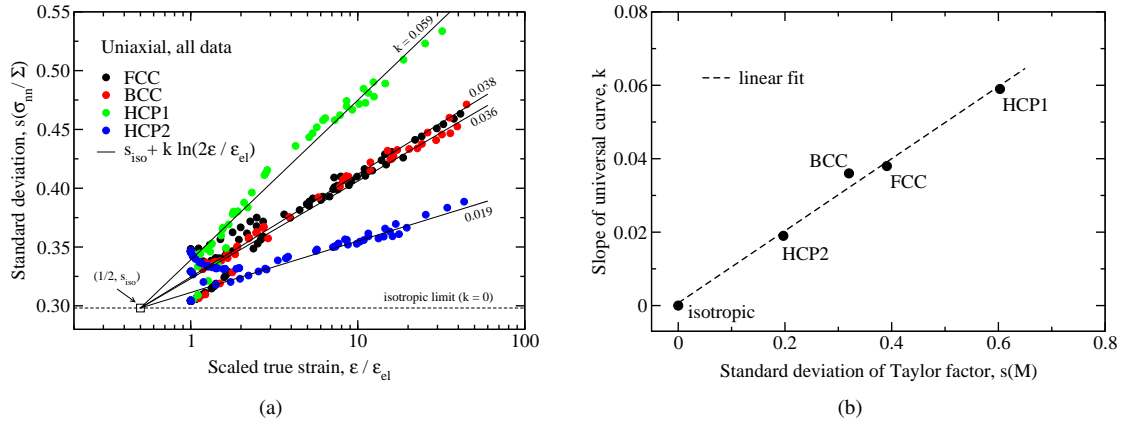


Figure 11. (a) Standard deviation of normalized intergranular normal stress calculated with Voronoi finite element simulations as a function of applied strain rescaled by elastic strain assuming crystal elasticity and plasticity for various materials (from Tab. 1) and slip systems under uniaxial loading conditions. Solid lines represent linear fits (in terms of  $\ln(\epsilon/\epsilon_{el})$ ) going through a common point denoted by a square. (b) Estimated slope of the log-like behavior,  $k$  in Eq. 12, versus standard deviation of Taylor factor,  $s(M)$ , under uniaxial loading conditions.  $k$  is taken from the fits in (a) and  $s(M)$  is calculated for a 1000-grain Lin model (*i.e.*, polycrystal with assumed uniform total strain) assuming crystal elasticity and ideal plasticity.

Combining the results from Secs. 3.1 and 3.2 leads to the following estimation of the standard deviation of intergranular normal stress distribution in untextured aggregates under uniaxial loading conditions

$$s(\sigma_{nm}/\Sigma) \approx \begin{cases} \frac{4}{3\sqrt{5}} \frac{A^u + 6}{A^u + 12} & ; \epsilon \leq \epsilon_y \\ \frac{2}{3\sqrt{5}} + 0.10s(M) \ln\left(\frac{2\epsilon}{\epsilon_{el}}\right) & ; \text{otherwise} \end{cases} \quad (14)$$

where the first equation corresponds to the elastic anisotropy described through the universal anisotropy index  $A^u$  proposed by (Ranganathan and Ostaja-Starzewski, 2008) and the second equation relates to the plastic anisotropy described through Taylor factor  $M$  and macroscopic ratio  $\epsilon/\epsilon_{el}$ . As shown in Figs. 11a and b, Eq. (14) allows to (accurately) estimate the width of the intergranular normal stress distribution under tensile loading from well-known macroscopic values: macroscopic stress  $\Sigma$ , macroscopic total strain

$\epsilon$ , macroscopic elastic strain  $\epsilon_{el}$  and standard deviation of Taylor factor  $s(M)$  (see Tab. E.7 in Appendix E). As  $s(\sigma_{nm}/\Sigma)$  is directly related to the shape of pdf (exactly for normal distribution, approximately for other kind of distributions), the estimated  $s(\sigma_{nm}/\Sigma)$  can be used to calculate, *e.g.*, the ratio of grain boundaries in a model with normal stress larger than some critical stress, as detailed in the conclusion section. This could lead to a powerful tool for quick and reliable estimation of material potential susceptibility to IGSCC initiation without actually performing finite element simulations.

#### 4. Discussion

It is the purpose of this section to elaborate further on the observed universality and to perform sensitivity analyses to establish the limits of its validation. In most cases presented hereafter only intergranular normal stresses under uniaxial loading conditions will be discussed, but it has been checked that similar conclusions can be drawn also for equibiaxial loading conditions.

##### 4.1. Sensitivity to the aggregate size

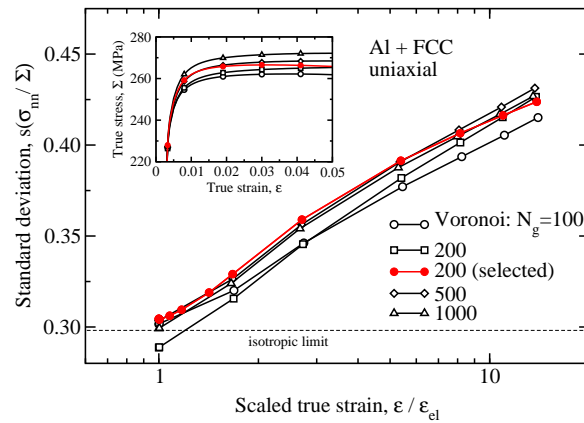


Figure 12. Standard deviation of normalized intergranular normal stress as a function of applied strain rescaled by elastic strain calculated for different Voronoi models ( $N_g$  denotes the number of grains), assuming crystal elasticity and ideal plasticity for Al and FCC under uniaxial loading conditions. Two aggregates with  $N_g = 200$  share the same number of grains but different grain topologies and orientations: the model shown in red is selected to be the representative model in this study. Inset: tensile response.

In Fig. 12 finite size analysis is performed with respect to different Voronoi aggregate models used in the calculation of standard deviation  $s(\sigma_{nm}/\Sigma)$ . Four different aggregate sizes, measured in terms of the number of grains  $N_g$ , are studied and compared using random orientations for the grains and approximately same mesh density of finite element discretization (*i.e.*,  $\sim 1300$  elements per grain), see Tab. 3. For one aggregate size ( $N_g = 200$ ), however, two different grain topologies and mesh densities are compared in addition.

$N_g$	$N_e$	$N_e/N_g$
100	133k	1330
200	271k	1355
200	396k	1980
500	685k	1370
1000	1355k	1355

Table 3. A list of Voronoi aggregate models used in the finite size analysis. Aggregates of cubic shape are composed of  $N_g$  grains of random orientations and meshed by  $N_e$  tetrahedral quadratic elements (C3D10 in Abaqus). The model with  $N_g = 200$  and  $N_e = 396k$  (*i.e.*,  $\sim 2000$  elements per grain) is used as the representative model throughout this study.

In Fig. 12 a maximum scatter of  $\sim 0.02$  (or  $\sim 6\%$ ) is observed among the five resulting  $s(\sigma_{nm}/\Sigma)$  evolutions. The results obtained for  $N_g = 500$  and  $1000$  grains seem to be already converged on a given scale, while moderate fluctuations can still be observed for  $N_g = 100$  and  $200$  models. However, the model with  $N_g = 200$  grains and  $N_e/N_g = 1980$  elements per grain (shown in red in Fig. 12) provides a very similar response as the larger two models. This model has therefore been selected to be the representative model in this study.

#### 4.2. Free surface effects: Application to stress-corrosion cracking

The probability density functions presented so far were obtained by post-processing entire aggregates, *i.e.*, independently of the location of the grain boundaries with respect to the distance from the free surface. As stress corrosion cracking initiates at free surface, the *pdfs* of intergranular stresses close to free surface are calculated and presented in this section. A comparison is made in a fully plastic regime at  $\epsilon = 0.05^4$  using the entire aggregate model and outer sections of the model where grain boundaries are located close to a free surface within distance  $r$ . The case with Al elasticity and FCC ideal plasticity is considered in the calculation of *pdfs*.

<sup>4</sup>Note that macroscopic strain of 0.05 is sufficient to describe SCC initiation in most of the experimental cases.

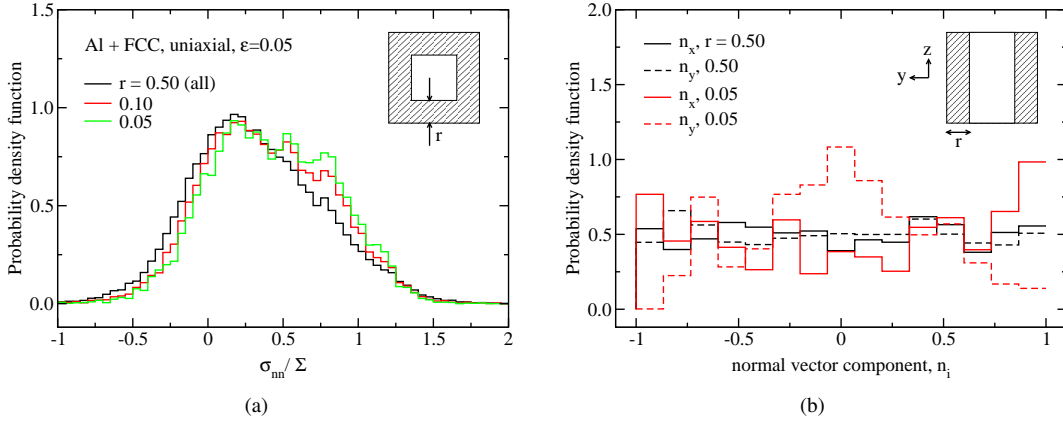


Figure 13. (a) Probability density functions of normalized intergranular normal stress calculated on grain boundaries with a maximum distance  $r$  from a free surface ( $r = 0.5$  denotes entire aggregate). Voronoi finite element simulations were performed for  $\epsilon = 0.05$  assuming crystal elasticity and ideal plasticity for Al and FCC under uniaxial loading conditions. (b) Probability density functions of grain boundary normal components  $n_x$  and  $n_y$  calculated within the entire aggregate ( $r = 0.5$ ) and within a thin outer layer ( $r = 0.05$ ) facing the free surface in Y direction (note that tensile loading is assumed in X direction).

In Fig. 13(a) the free surface effects are manifested mostly in bulk stress region by the appearance of additional peaks at  $\sigma_{mn}/\Sigma \sim 0.5$  and  $0.8$ . However, the upper tail of *pdfs*, relevant for IGSCC initiation, is not considerably affected. The corresponding differences in mean and standard deviation of intergranular normal stress are listed in Tab. 4

$r$	$\langle \sigma_{mn}/\Sigma \rangle$	$s(\sigma_{mn}/\Sigma)$
0.50	0.335	0.445
0.10	0.401	0.421
0.05	0.440	0.409

Table 4. Mean and standard deviation of intergranular normal stress distributions from Fig. 13(a).

The observed changes in Fig. 13(a) and Tab. 4 may be attributed to two different causes. The first one can be related to the transition from bulk (3D) to plane (2D) stress state realized at a free surface where softer material response is expected due to fewer constraints applied there. However, this effect has been estimated to be relatively small and should affect the *pdf* only in the  $\sigma_{mn} \sim 0$  region.

The second cause can be connected to topology changes of the grain boundaries when approaching free surfaces from the bulk. The fact that grain boundary topology evolves with  $r$  is confirmed in Fig. 13(b) by showing extracted distributions of grain boundary normal components  $n_x$  and  $n_y$  from the (undeformed) Voronoi model. An expected uniform distribution is observed for both  $n_x$  and  $n_y$  when accounting for the entire aggregate ( $r = 0.5$ ), while a non-uniform distribution is clearly developed when considering grain boundaries located within a thin outer layer ( $r = 0.05$ ). This evolution is a consequence of using Voronoi model generator which, by default, avoids making sharp corners between the grain boundaries and free surfaces. In this way, small and highly distorted finite elements are avoided in the discretization of the model. As a result, hence, practically no grain boundaries parallel to the free surfaces are generated on the outer most region of the aggregate.

In realistic aggregates, however, grain (boundary) topology of the free-surface region should not differ

considerably from the one existing in the bulk (neglecting the effects of sample surface preparation). Therefore, negligible free-surface effects are expected in the *pdfs* of realistic polycrystals. This suggests that results obtained for the bulk aggregates (Sec. 3) can as well be used to describe the stress distributions close to the free surfaces, and therefore be used to model IGSCC initiation.

Strong influence of the grain topology (as well as overall texture) on the evolution of the *pdfs* was highlighted also in (Hure et al., 2016).

#### 4.3. Deviations from universal plastic behavior

The universal behavior for the evolution of standard deviation of normalized intergranular normal stress with strain described in Section 3.2 and modeled through Eq. (14) has been proposed to arise solely from grain-grain interactions resulting from grain anisotropy. At higher ratios of  $\epsilon/\epsilon_y$  the observed universal behavior may no longer be valid. This limit is investigated and demonstrated in Fig. 14 where additional simulations have been performed for sets of material properties leading to very small values of yield strain (corresponding to the limit of rigid-plastic materials), therefore in the limit  $\epsilon/\epsilon_y \gg 1$ , while keeping the macroscopic strain small ( $\epsilon \leq 0.05$ ) and grain orientations fixed at zero texture. In this way, the effects of geometry and texture evolution have been avoided. The universality of the evolution of  $s(\sigma_{nn}/\Sigma)$  with strain for different standard deviations of Taylor factor,

$$s(\sigma_{nn}/\Sigma) = s_{iso} + \alpha s(M) \mathcal{F} \left( \frac{\epsilon}{\epsilon_y} \right) \quad (15)$$

is retained up to  $\epsilon/\epsilon_y \sim 1000$ , but with function  $\mathcal{F}$  well approximated by square-root rather than log-like behavior observed for lower values of  $\epsilon/\epsilon_y$  (Eq. (14)). While Eq. (15) has been established for the conditions used in Fig. 14, such high values of  $\epsilon/\epsilon_y$  are not likely to occur in practical situations, and deviations from Eq. (14) are likely to develop at large strains. The purpose of the following two subsections is thus to describe the conditions under which the deviations from Eq. (14) are observed.

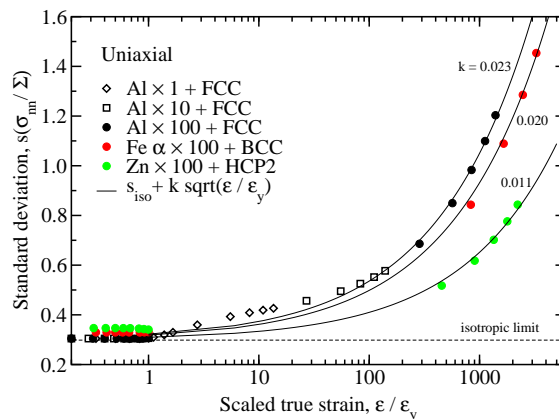


Figure 14. Standard deviation of normalized intergranular normal stress calculated with Voronoi finite element simulations as a function of applied strain rescaled by yield strain assuming crystal elasticity and ideal ( $H = 0$ ) plasticity for various materials (with rescaled elastic properties - by factor 10 or 100) and slip systems under uniaxial loading conditions. Solid lines represent square-root fits of Eq. (15) on data points with  $\epsilon/\epsilon_y > 100$ . The simulations were performed using small deformation theory (*i.e.*, fixed orientations) with corresponding maximum strain of 0.05.

### 4.3.1. Deviations due to geometrical changes

At large strains the assumptions of zero texture and random grain shapes become no longer valid. The geometrical changes (elongation of the grains) as well as the generation of small non-zero texture may affect the universal *pdf* behavior of the intergranular stresses in the plastic regime described in Sec. 3. Large strain simulations have thus been performed to assess the strain above which universal log-like behavior starts to fail. A case with Al elasticity and FCC plasticity with finite hardening ( $H = 500$  MPa) is considered for uniaxial loading conditions with strains up to  $\epsilon \sim 0.4$ .

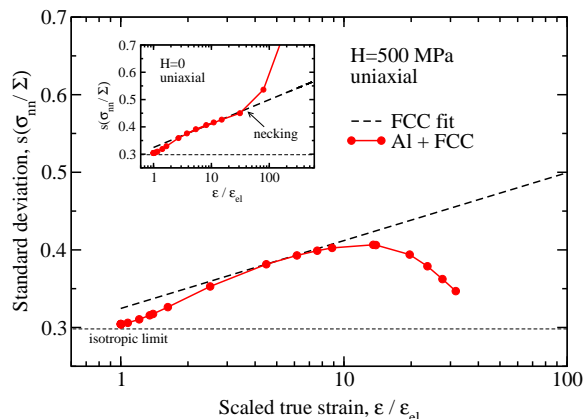


Figure 15. Standard deviation of normalized intergranular normal stress calculated with Voronoi finite element simulation as a function of applied strain (up to  $\epsilon \sim 0.4$ ) rescaled by elastic strain assuming crystal elasticity and plasticity for Al and FCC with finite hardening strength  $H=500$  MPa (inset:  $H=0$ ) under uniaxial loading conditions. The fitted logarithmic curve for FCC from Fig. 11(a) is shown for comparison.

The results shown in Fig. 15 indicate that logarithmic behavior of  $s(\sigma_{nn}/\Sigma)$  is retained up to  $\epsilon/\epsilon_{el} \sim 10$ , which corresponds to  $\epsilon \sim 0.06$ . Beyond this strain a down-turn of  $s(\sigma_{nn}/\Sigma)$  is observed which can be attributed to the accumulated changes of grain shapes (grain elongations) as well as crystallographic texture evolution.

With the evolution of texture the misorientations between neighboring grains become smaller on average<sup>5</sup>, which reduces the mismatch effects (and thus the stresses) between adjacent grains. It is important to note that finite hardening modulus ( $H = 500$  MPa) is used in the simulation to avoid the initiation of macroscopic necking. In this way the stress state is kept uniaxial in the entire model domain for all  $\epsilon \lesssim 0.4$ .

In the inset of Fig. 15, however, a similar analysis but with zero hardening ( $H = 0$ ) is performed to study the large-strain response of the ideally plastic material. The observed up-turn of  $s(\sigma_{nn}/\Sigma)$  at  $\epsilon/\epsilon_{el} \sim 30$  (or  $\epsilon \sim 0.1$ ) is attributed here mostly to the initiation of macroscopic necking. At the onset of necking the macroscopic stress  $\Sigma$  starts to decrease with further straining due to strong reorientations of the grains in the necking region. The effect of  $\Sigma$  decline with strain is strong enough to result in the up-turn of  $s(\sigma_{nn}/\Sigma)$ .

Note that both uniaxial and equibiaxial loading conditions provide the same qualitative behavior of  $s(\sigma_{nn}/\Sigma)$  with strain.

<sup>5</sup> In the extreme limit of fully developed texture the misorientations between the grains become zero as all the grains share the same orientation.

#### 4.3.2. Deviations from Taylor hardening

The influence of different hardening models on the observed universal behavior of  $s(\sigma_{nn}/\Sigma)$  with  $\epsilon/\epsilon_{el}$  (see, e.g., Fig. 10) is investigated in Fig. 16(a) for Al and FCC and in Fig. 16(b) for Zn and HCP2 under uniaxial loading conditions. In addition to linear Taylor hardening, Eq. (3), two more realistic hardening models are introduced: an empirical hardening model of Peirce, Asaro and Needleman (PAN) (Peirce et al., 1983), used to describe Stage I hardening in FCC metals, where

$$\tau_c^\alpha = \tau_0 + \int \sum_{\beta} h_{\alpha\beta} |\dot{\gamma}^\beta| dt \quad \text{with} \quad h_{\alpha\alpha} = H \operatorname{sech}^2\left(\frac{H}{\tau_s - \tau_0} \Gamma\right) \quad \text{and} \quad h_{\alpha\beta} = q h_{\alpha\alpha} \quad (\alpha \neq \beta), \quad (16)$$

and a recently introduced physics-based hardening model of Han (Han, 2012), used to describe the behavior of (non-irradiated) austenitic stainless steel in (Han, 2012; Hure et al., 2016), where

$$\tau_c^\alpha = \tau_0 + \mu \sqrt{\sum_{\beta} a^{\alpha\beta} r_D^\beta} \quad \text{with} \quad r_D^\alpha = \left( \frac{1}{\kappa} \sqrt{\sum_{\beta} b^{\alpha\beta} r_D^\beta} - G_c r_D^\alpha \right) |\dot{\gamma}^\alpha|. \quad (17)$$

With respect to Taylor hardening, two additional parameters are introduced in PAN model, Eq. (16):  $\tau_s$  denotes saturation shear stress and  $q$  a ratio of latent to self hardening. In the limit of  $q = 1$  and  $H\Gamma/(\tau_s - \tau_0) \ll 1$ , PAN model simplifies to Taylor hardening model.

The hardening model of Han, Eq. (17), accounts for dislocation density evolution (with corresponding normalized variable  $r_D^\alpha$ ). Parameter  $\mu$  is macroscopic shear modulus,  $a^{\alpha\beta}$  and  $b^{\alpha\beta}$  are dislocation interaction matrices composed of six independent parameters ( $a_i$  and  $b_i$ , for  $i = 1, \dots, 6$ ),  $\kappa$  is a value proportional to the number of obstacles crossed by a dislocation before being immobilized and  $G_c$  is a proportional factor that depends on the annihilation mechanism of dislocation dipoles (Han, 2012).

The hardening constitutive equations were implemented numerically into finite element solvers Abaqus (Simulia, 2016) and Cast3M (CEA, 2015). Both implementations have been shown to give equivalent results. The parameters of the three hardening models used in Fig. 16(a) are listed in Tab. 5.

Model	$\tau_0$	$\tau_s$	$H$	$q$	$\mu$	$\kappa$	$G_c$	$a_1$	$a_2$	$a_3$	$a_4$	$a_5$	$a_6$	$b_i$
Taylor	100		200											
PAN	100	200	200	0										
PAN	100	200	200	1										
PAN	100	200	200	2										
Han	88				65.6	42.8	10.4	0.124	0.124	0.070	0.625	0.137	0.122	$1 - \delta_{i1}$

Table 5. Hardening parameters used in Fig. 16(a). Parameters  $\tau_0$ ,  $\tau_s$  and  $H$  are shown in units of MPa, parameter  $\mu$  in units of GPa. Parameters of Han model correspond to 304L stainless steel (Hure et al., 2016).

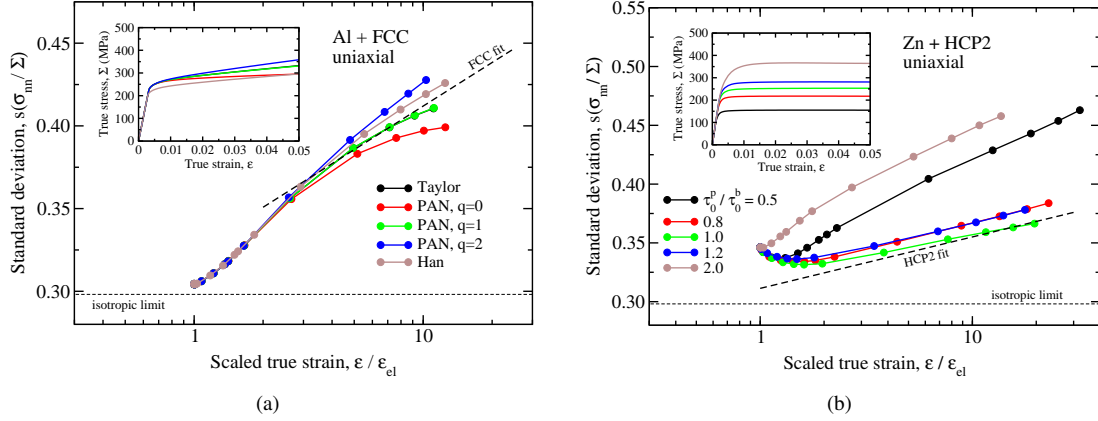


Figure 16. Standard deviation of normalized intergranular normal stress (inset: macroscopic tensile stress) as a function of applied strain rescaled by elastic strain calculated with Voronoi finite element simulations assuming crystal elasticity and plasticity for (a) Al and FCC with various hardening models under uniaxial loading conditions (see the text for models definitions and material parameters used in simulations) and (b) Zn and HCP2 with ideal ( $H = 0$ ) plasticity but with different ratios of initial critical resolved shear stresses  $\tau_0^{pyr}/\tau_0^{bas}$  (assuming  $\tau_0^{pri} = \tau_0^{pyr}$  and  $\tau_0^{bas} = 100$  MPa). The fitted logarithmic curves for FCC and HCP2 from Fig. 11(a) are shown for comparison.

A comparison of the three hardening models presented in Fig. 16(a) shows that universality of  $s(\sigma_{nm}/\Sigma)$  is maintained for all models up to  $\epsilon/\epsilon_{el} \sim 5$  where larger discrepancies from log-like behavior start to develop. In this respect, the  $q$  value is identified as the most influencing parameter of PAN model<sup>6</sup>. For  $q = 1$  a Taylor-like hardening is restored which results in almost identical  $s(\sigma_{nm}/\Sigma)$  curves. In this limit all slip systems experience the same strength, while the balance among slip systems is lost when  $q \ll 1$  or  $q \gg 1$ . This is manifested as down-turn or up-turn of the  $s(\sigma_{nm}/\Sigma)$  curve at  $\epsilon/\epsilon_{el} \gtrsim 5$ . Such deviations from Eq. (14) are in fact expected as the standard deviation of Taylor factor, which is the key parameter of Eq. (14), was computed assuming same ( $\alpha$ -independent) critical resolved shear stress for all slip systems. For  $q \ll 1$  or  $q \gg 1$  such assumption breaks down. However, it should be noted that typical values for common cubic materials, like austenitic stainless steel, have been reported to be in the range of  $1 \leq q < 2$  (El Shawish and Cizelj, 2017), implying that a reasonably good agreement with observed universal log-like behaviour can be expected in this material.

The same reasoning may be used to justify the similar responses of Han and Taylor hardening models observed in Fig. 16(a). Since all the terms but one of the dislocation interaction matrix  $a^{\alpha\beta}$  in Han model are close to one single value ( $\sim 0.1$ , see Tab. 5), the critical resolved shear stress may be approximated as  $\alpha$ -independent,  $\tau_c^\alpha \sim \tau_0 + \mu \sqrt{0.1 \sum_\beta r_D^\beta}$ . In this way, slip systems in Han model should experience similar strengths, like in  $q \sim 1$  case of PAN model.

To account for even larger plastic anisotropy distinctive of realistic hcp materials, the influence of non-uniform initial critical resolved shear stress,  $\tau_0 = \mathcal{F}(\alpha)$ , is studied in Fig. 16(b). As an illustrative example, Zn elasticity with HCP2 ideal plasticity is addressed with different  $\tau_0$  values for basal, prismatic and pyramidal second order slip modes defined in Tab. 2. Following the approach in (Lebensohn et al., 2007), a single contrast parameter is introduced, descriptive of the single crystal plastic anisotropy, given

<sup>6</sup> Note that same qualitative results are obtained also with Bassani and Wu hardening model (Bassani and Wu, 1991) which accounts for Stage I and II hardening.

by the ratio of the initial critical resolved shear stress between pyramidal (assumed here to be equal to prismatic) and basal slip modes,  $\tau_0^{pyr}/\tau_0^{bas}$ . Although  $\tau_0^{pyr}/\tau_0^{bas} > 50$  in some single hcp crystals (*e.g.*, 48–96 for Mg (Hutchinson and Barnett, 2010)), the ratio is usually greatly reduced in polycrystalline arrangement (*e.g.*, 2–5 for Mg (Hutchinson and Barnett, 2010)), as explained in (Hutchinson and Barnett, 2010). In this view, a close vicinity of the uniform case,  $0.5 \leq \tau_0^{pyr}/\tau_0^{bas} \leq 2.0$ , is investigated in Fig. 16(b). While a uniform-like response is reproduced for relatively small (up to  $\sim 20\%$ ) variations in  $\tau_0$ , the results for moderate  $\tau_0^{pyr}/\tau_0^{bas} = 0.5$  and 2.0 already demonstrate substantial deviations of the calculated intergranular normal stresses from the proposed HCP2 universal behavior. In order to extend the validity of Eq. (14), to apply also for the general realistic hcp polycrystal, the non-uniformity of  $\tau_0$  would need to be considered also in Taylor factor calculation. This is left for future investigations.

Following the results presented in Fig. 16, it is reasonable to assume that universal log-like behavior of  $s(\sigma_{mn}/\Sigma)$  with  $\epsilon/\epsilon_{el}$ , proposed and demonstrated in Sec. 3 for Taylor hardening, applies also for other more sophisticated hardening laws as long as they provide a uniform (or close to uniform) strength evolution among the slip systems.

## 5. Conclusions

Intergranular normal stresses are likely to be one of the key ingredients required for quantitative modeling of intergranular stress corrosion cracking (IGSCC) of polycrystalline materials. Crystal plasticity finite element simulations have been performed in order to assess the distributions of intergranular normal stresses as a function of elastic and plastic properties at the grain scale for two different macroscopic loading conditions. Untextured Voronoi aggregates have been considered with initially equiaxed grain shapes and random crystallographic orientations, under relatively low applied strain. Moreover, small variations in the initial critical resolved shear stress have been assumed among different slip systems, with self and latent hardening being of the same order of magnitude. A wide variety of elastic/plastic properties have been studied. Although not covering all the situations where IGSCC phenomenon is observed experimentally, the investigated conditions are relevant to a wide class of problems where IGSCC initiation is involved, for example, to austenitic stainless steels or nickel-based alloys.

Depending on material properties, complex intergranular normal stress distributions have been obtained and characterised through their first two statistical moments, *i.e.*, mean and standard deviation. For all simulations presented in this study, the mean normal stress remains approximately constant at  $\Sigma/3$  (*resp.*  $2\Sigma/3$ ) for uniaxial (*resp.* equibiaxial) loading conditions, where  $\Sigma$  characterizes the macroscopic stress amplitude. Standard deviation normalized by macroscopic stress has been shown to depend only on elastic properties for applied strain below the macroscopic yield strain, and only on plastic properties in fully plastic regime when plotted as a function of applied strain rescaled by elastic strain. The evolution of the standard deviation during the transition between the elastic regime and fully plastic regime depends on both elastic and plastic properties, leading to an increase or decrease depending on the relative measure of elastic *vs.* plastic anisotropy.

In the elastic regime, a simple correlation has been found and explained through simple arguments between the standard deviation of intergranular normal stress and a universal anisotropy index recently proposed. In the plastic regime, the standard deviation increases with strain due to grain-grain interactions resulting from plastic anisotropy. The increasing behavior of standard deviation with strain has been found to be decoupled into (i) a strain-independent part that correlates linearly with the standard deviation of Taylor factor characterizing the slip systems and (ii) a universal strain-dependent function. A simple phenomenological formula (Eq. (14)) has been proposed that captures well all the numerical data obtained in this study.

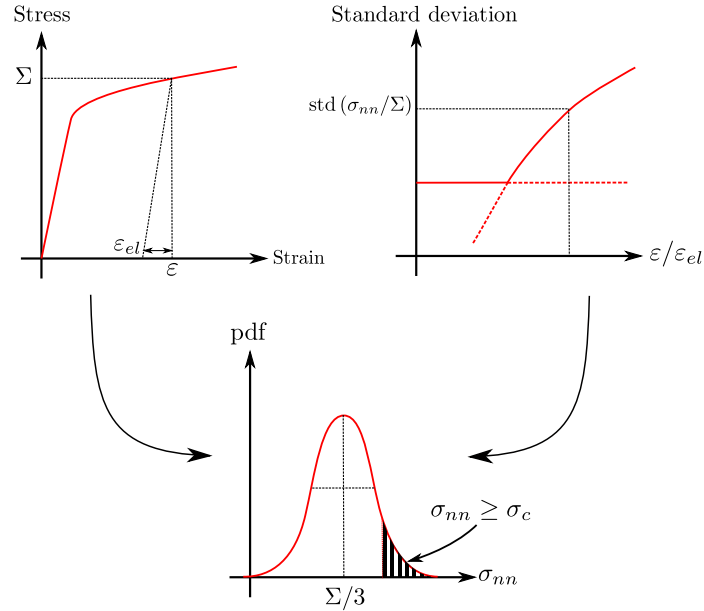


Figure 17. Methodology for estimating the probability of finding intergranular normal stress higher than a critical value based on the knowledge of the material properties and Eq. (14).

As shown in Fig. 17, this formula leads to an easy tool to estimate the intergranular normal stresses in a polycrystalline aggregate. Knowing the single crystal elastic properties and standard deviation of Taylor factor (for most cases tabulated in reference textbook) as well as the loading applied to the material (macroscopic stress and strain), standard deviation of normalized intergranular normal stress can be readily obtained, leading to an estimate of the probability density function of the intergranular stress. The probability of finding a stress higher than a critical value (related to grain boundary strength) can finally be assessed. Such approach can be used to quickly and reliably estimate the propensity of an aggregate to develop high intergranular normal stresses without having to perform finite element simulations and/or to build an IGSCC fracture model once knowing the grain boundary strength.

As a working example of this approach, IGSCC results presented in (Zhou et al., 2009) of (un-)irradiated austenitic stainless steel tested in supercritical water are used. This study reports crack lengths per unit area under uniaxial loading conditions after slow strain rate tests, as a function of strain and irradiation levels (that correspond at first approximation to different yield stresses of the material) (Fig. 18). Crack lengths reported are close to the grain size, so that these data correspond mainly to IGSCC initiation regime. Under the assumption of normal distribution, the probability of finding intergranular normal stress higher than a critical stress  $\sigma_c$  can be expressed as  $P_f(\sigma_{nn}/\Sigma \geq \sigma_c/\Sigma) = 1/2 \operatorname{erfc}[(\sigma_c/\Sigma - 1/3)/\sqrt{2}std]$ , where  $\operatorname{erfc}$  is the complementary error function,  $\Sigma$  the macroscopic stress, and  $std$  the standard deviation as given by Eq. (14). This probability is assumed to be the fraction of grain boundaries subjected to normal stress higher than  $\sigma_c$ , which leads to an estimation of the crack length per unit area  $G_f P_f$ , where  $G_f$  is the grain boundary length per unit area. Figure 18 shows that a constant  $\sigma_c$  is able to capture the trend of the data presented in (Zhou et al., 2009) for both dependence on strain and irradiation (hardening) levels. Although in this example critical grain boundary stress might also depend on irradiation as a result of microchemistry modification (which might explain the discrepancy observed in Fig. 18) as well as the rather high strain level, such

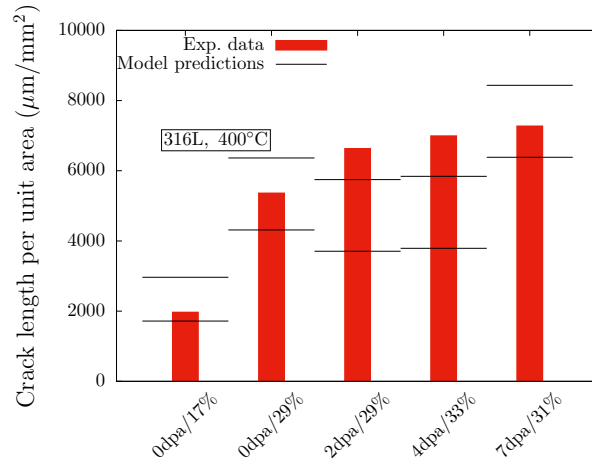


Figure 18. Crack length per unit area for different irradiation levels/applied strain (Zhou et al., 2009). Numerical predictions have been computed assuming an applied true stress of [455 – 515] MPa and [555 – 630] MPa at the unirradiated state (denoted 0 dpa) (corresponding to the stress range for conventional strain of 17% and 29% on the tensile curves given in (Zhou et al., 2009)). For the irradiated materials (2/4/7 dpa), the applied true stress is set equal to the yield stress computed as the sum of the yield stress of the unirradiated material at test temperature (~180 MPa) and the irradiation hardening reported in (Zhou et al., 2009) (as low strain-hardening is expected for such material). This leads to applied true stress of [530 – 610] MPa and [630 – 710] MPa for the 2/4 dpa and 7 dpa irradiation levels. The grain boundary length per unit area is approximated by  $G_f \approx 2/\phi$ , where  $\phi$  is the grain size. The critical stress  $\sigma_c$  was calibrated to a value of 550 MPa.

comparison appears promising and call for further assessment of this methodology.

In addition, the standard deviations obtained in this study could be easily used to improve the IGSCC model developed recently by Couvant *et al.* (Couvant et al., 2018; Couvant, 2018). This model, that describes the incubation, initiation and propagation stages of IGSCC, has been shown to give promising results once calibrated on Nickel based alloy 600. The initiation phase modeling uses standard deviation of intragranular axial stress (under uniaxial tensile conditions) computed through CPFEM simulations, and assuming that the upper tail is somehow related to grain boundaries perpendicular to the loading directions where high stresses are expected to occur. A critical stress is then calibrated based on experimental data. The main drawback of this approach is that the physical meaning of this critical stress may not be so obvious – as how this critical stress is related to grain boundary fracture energy ? – that would be clearer when using the standard deviations of intergranular normal stress obtained in this study.

Although Eq. (14) captures well most of the numerical data presented in this study, the theoretical justification of the evolution of the standard deviation of intergranular normal stress with strain remains an open question. Moreover, the effects of a general non-uniform critical resolved shear stress distribution, unloading and texture (either from initial crystallographic orientations/grain shapes or induced by deformation/hardening), relevant for specific applications, are still to be further assessed, which is left for future work.

## Acknowledgments

The authors acknowledge the financial support from Slovenian Research Agency and French Atomic Energy Commission through the bilateral project “Towards quantitative predictions of stress corrosion cracking

initiation stress threshold for PWR's internals", No. BI-FR/CEA/15-17-007, between CEA and JSI in years 2015-2017.

### Appendix A. Influence of loading conditions on intergranular stress distributions

In this study, tensile loading is simulated by applying an incremental tensile displacement along the  $X$  axis to all the nodes on the front surface of the Voronoi model, while keeping the nodes on the back surface constrained to have zero axial displacement (for equibiaxial loading also the  $Y$  axis is loaded in the same manner). Such loading conditions keep the opposite surfaces flat, thus providing additional (unwanted) stresses close to these surfaces.

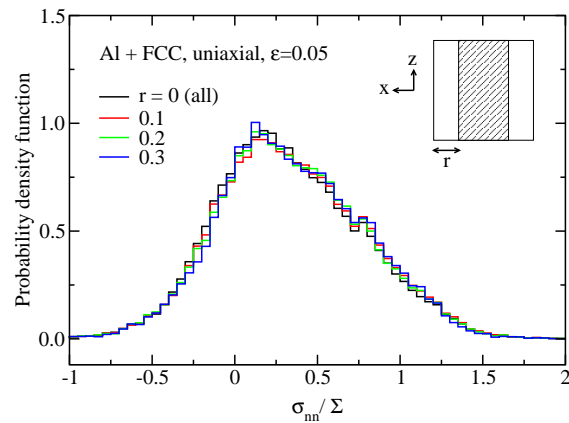


Figure A.19. Probability density functions of normalized intergranular normal stress calculated on grain boundaries with a minimum distance  $r$  from the loading surfaces ( $r = 0$  denotes entire aggregate). Voronoi finite element simulations were performed for  $\epsilon = 0.05$  assuming crystal elasticity and ideal plasticity for Al and FCC under uniaxial loading conditions.

Figure A.19 shows the influence of such loading conditions on the intergranular normal stress distributions when calculated away (by distance  $r$ ) from the loading surfaces. Practically no effects can be observed on the distributions for the increasing  $r$ . It is therefore confirmed that proposed loading conditions have negligible effects on the results presented in this study.

## Appendix B. Comparison of different approaches to calculate intergranular stress

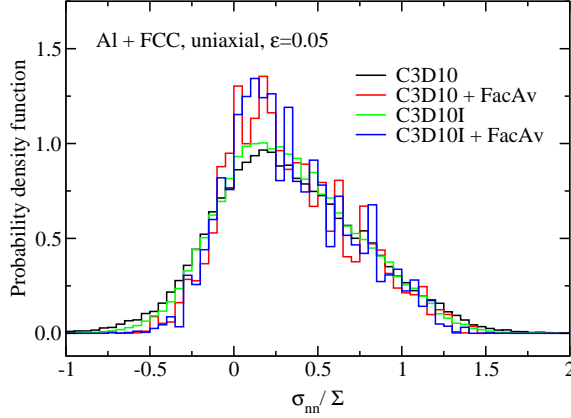


Figure B.20. Probability density functions of normalized intergranular normal stress calculated with Voronoi finite element simulations at  $\epsilon = 0.05$  assuming crystal elasticity and ideal plasticity for Al and FCC under uniaxial loading conditions. The curves correspond to different methods used to obtain intergranular normal stress. Same aggregate model is used in all cases. Legend: C3D10: at closest Gauss points using standard tetrahedral element C3D10; C3D10I: at Gauss points exactly at the intergranular position using special tetrahedral element C3D10I; FacAv: averaging on grain facet using weights from triangular element areas.

Figure B.20 shows a comparison between different strategies in obtaining intergranular normal stresses. Relatively small differences are observed between calculated *pdfs* when using C3D10 or C3D10I tetrahedra. When using a special tetrahedral element C3D10I with 10 Gauss points positioned at the nodes (and 1 at the element center), the projected stresses may be obtained exactly at grain boundaries. However, as grain boundary node is usually shared by several tetrahedra (associated tetrahedra can either share a common grain boundary facet, edge or node), additional (weighted) averaging of the stresses may be needed in order to obtain a unique stress value per grain boundary node. This brings some ambiguity to intergranular stress calculation. For this reason and since the differences between using C3D10 and C3D10I tetrahedra are small, C3D10 tetrahedra have been used through the paper to calculate the *pdfs*.

Figure B.20 also shows the effect of using an additional grain-facet averaging, used *e.g.* in (Gonzalez et al., 2014), where only one stress value is retained per grain facet. In this way, extreme local intergranular stresses average out to produce (slightly) narrower *pdf* but with retained global shape. Also, as the number of grain facets is much smaller than the number of element pairs on the grain boundaries, larger aggregate models would be needed to obtain smoother distributions. For this reason no additional averaging over grain facets has been used throughout the paper to calculate the *pdfs*.

## Appendix C. Intergranular normal stress distribution in polycrystal with isotropic grains

In a polycrystal with isotropic grains local stress  $\sigma$  is uniform and equal to the applied stress  $\Sigma$ . The intergranular normal stress may therefore be calculated as  $\sigma_{nn} = n \cdot \Sigma \cdot n$ , where  $n = (\sin \theta \sin \phi, \sin \theta \cos \phi, \cos \theta)$  is grain boundary normal written with spherical coordinates. Assuming diagonal stress state,  $\Sigma = \Sigma_{xx} e_X \otimes e_X + \Sigma_{yy} e_Y \otimes e_Y + \Sigma_{zz} e_Z \otimes e_Z$ , the intergranular normal stress becomes  $\sigma_{nn} = \Sigma_{zz} \cos^2 \theta + \sin^2 \theta (\Sigma_{xx} \cos^2 \phi + \Sigma_{yy} \sin^2 \phi)$ , which simplifies to

$$\sigma_{nn} = \Sigma \cos^2 \theta \quad \text{and} \quad \sigma_{nn} = \Sigma \sin^2 \theta \quad (\text{C.1})$$

for, respectively, tensile ( $\Sigma = \Sigma_{zz}$ ,  $\Sigma_{xx} = \Sigma_{yy} = 0$ ) and equibiaxial loading ( $\Sigma = \Sigma_{xx} = \Sigma_{yy}$ ,  $\Sigma_{zz} = 0$ ).

To calculate the distribution function of  $\sigma_{nn}/\Sigma$ ,  $f_2(\sigma_{nn}/\Sigma)$ , it is assumed that  $\cos \theta$  is distributed uniformly,  $f_1(\cos \theta) = 1$ , on a range  $0 \leq \cos \theta \leq 1$  (the negative values of  $\cos \theta$  can be omitted without loss of generality since  $n$  and  $-n$  denote the same grain boundary). This corresponds to a polycrystal with random grain boundary topology or random grain shapes (with no preferred direction).

Following the theorem of change of variables,  $f_1(x_1)|dx_1| = f_2(x_2)|dx_2|$ , where  $x_1 = \cos \theta$ ,  $x_2 = \sigma_{nn}/\Sigma$  and  $f_1(x_1) = 1$ , the distribution function becomes  $f_2(\sigma_{nn}/\Sigma) = |d(\cos \theta)/d(\sigma_{nn}/\Sigma)|$ . Writing  $\cos \theta = \sqrt{\sigma_{nn}/\Sigma}$  for tensile and  $\cos \theta = \sqrt{1 - \sigma_{nn}/\Sigma}$  for equibiaxial loading, respectively,

$$f_2(\sigma_{nn}/\Sigma) = \frac{1}{2\sqrt{\sigma_{nn}/\Sigma}} \quad \text{and} \quad f_2(\sigma_{nn}/\Sigma) = \frac{1}{2\sqrt{1 - \sigma_{nn}/\Sigma}} \quad (\text{C.2})$$

on a range  $0 \leq \sigma_{nn}/\Sigma \leq 1$ .

#### Appendix D. Universal elastic anisotropy index calculation

The universal elastic anisotropy index is calculated as (Ranganathan and Ostaja-Starzewski, 2008)

$$A^u = 5 \frac{G^V}{G^R} + \frac{K^V}{K^R} - 6 \quad (\text{D.1})$$

where  $G$  and  $K$  denote shear and bulk moduli, and superscripts  $V$  and  $R$  represent the Voigt and Reuss estimates, respectively. In the following, the estimates for the elastic moduli are given for a quasi-isotropic polycrystal aggregate composed of randomly oriented grains whose size is small relative to the size of the polycrystal.

The general forms for  $K^V$  and  $G^V$  can be expressed as (Tromans, 2011)

$$\begin{aligned} K^V &= \frac{C_{11} + C_{22} + C_{33} + 2(C_{12} + C_{13} + C_{23})}{9} \\ G^V &= \frac{C_{11} + C_{22} + C_{33} + 3(C_{44} + C_{55} + C_{66}) - (C_{12} + C_{13} + C_{23})}{15} \end{aligned} \quad (\text{D.2})$$

where  $C_{ij}$  are stiffness matrix components in Voigt notation.

In a similar way, the general forms for  $K^R$  and  $G^R$  can be written as (Tromans, 2011)

$$\begin{aligned} K^R &= \frac{1}{S_{11} + S_{22} + S_{33} + 2(S_{12} + S_{13} + S_{23})} \\ G^R &= \frac{15}{4(S_{11} + S_{22} + S_{33}) + 3(S_{44} + S_{55} + S_{66}) - 4(S_{12} + S_{13} + S_{23})} \end{aligned} \quad (\text{D.3})$$

where  $S_{ij}$  denote compliance matrix components.  $S_{ij}$  are related to  $C_{ij}$  via matrix inversion.

Elastic moduli can be further simplified when accounting for the symmetries of the crystal lattice. For cubic symmetry,  $C_{11} = C_{22} = C_{33}$ ,  $C_{44} = C_{55} = C_{66}$  and  $C_{12} = C_{13} = C_{23}$ , the moduli can be expressed (solely with  $C_{ij}$ ) as

$$\begin{aligned} K^V &= \frac{C_{11} + 2C_{12}}{3} \\ G^V &= \frac{C_{11} + 3C_{44} - C_{12}}{5} \\ K^R &= K^V \\ G^R &= \frac{5C_{44}(C_{11} - C_{12})}{3C_{11} + 4C_{44} - 3C_{12}}, \end{aligned} \quad (\text{D.4})$$

while for hexagonal symmetry,  $C_{11} = C_{22}$ ,  $C_{44} = C_{55}$ ,  $C_{66} = (C_{11} - C_{12})/2$  and  $C_{13} = C_{23}$ , the moduli follow as

$$\begin{aligned}
K^V &= \frac{2C_{11} + C_{33} + 2C_{12} + 4C_{13}}{9} \\
G^V &= \frac{7C_{11} + 2C_{33} + 12C_{44} - 5C_{12} - 4C_{13}}{30} \\
K^R &= \frac{C_{33}(C_{11} + C_{12}) - 2C_{13}^2}{C_{11} + 2C_{33} + C_{12} - 4C_{13}} \\
G^R &= \frac{15C_{44}(C_{11} - C_{12})(C_{33}(C_{11} + C_{12}) - 2C_{13}^2)}{6(C_{11} - C_{12})(C_{33}(C_{11} + C_{12}) - 2C_{13}^2) + 2C_{44}(2C_{11}^2 - 2C_{12}^2 + 5C_{12}C_{33} + C_{11}(4C_{13} + 7C_{33}) - 4C_{13}(C_{12} + 3C_{13}))}.
\end{aligned} \tag{D.5}$$

Note that in isotropic limit (*i.e.*, cubic symmetry with  $C_{44} = (C_{11} - C_{12})/2$ ) Voigt and Reuss estimates become the same,  $K^V = K^R = (C_{11} + 2C_{12})/3$  and  $G^V = G^R = (C_{11} - C_{12})/2$ .

Material	Crystal system	$C_{11}$	$C_{12}$	$C_{13}$	$C_{33}$	$C_{44}$	$A^u$	$\tilde{A}^u$	$ \tilde{A}^u - A^u /A^u$
Al	FCC	107.3	60.9			28.3	0.048	0.051	0.077
Ni	FCC	246.5	147.3			127.4	1.149	1.171	0.019
Au	FCC	192.9	163.8			41.5	1.443	1.636	0.133
Cu	FCC	168.4	121.4			75.4	1.824	1.932	0.059
Pb	FCC	49.5	42.3			14.9	2.857	3.182	0.114
Nb	BCC	240.2	125.6			28.2	0.629	0.698	0.110
Fe $\alpha$	BCC	231.4	134.7			116.4	0.987	1.006	0.019
Li	BCC	13.5	11.44			8.78	7.970	8.272	0.038
Na	BCC	6.15	4.96			5.92	9.660	9.380	0.029
Mg	HCP	59.7	26.2	21.7	61.7	16.4	0.036	0.037	0.031
Be	HCP	292.3	26.7	14.0	336.4	162.5	0.048	0.042	0.121
Zr	HCP	143.4	72.8	65.3	164.8	32.0	0.108	0.115	0.059
Co	HCP	307.0	165.0	103.0	358.1	78.3	0.259	0.271	0.043
Cd	HCP	115.8	39.8	40.6	51.4	20.4	1.170	1.171	0.001
Zn	HCP	161.0	34.2	50.1	61.0	38.3	1.774	1.772	0.001

Table D.6. Elastic constants  $C_{ij}$  (in units of GPa) and universal elastic anisotropy index  $A^u$  and its approximation  $\tilde{A}^u$  of cubic (FCC, BCC) and hexagonal (HCP) single crystals used in this study. Elastic constants are taken from (Bower, 2010). Note that  $C_{33} = C_{11}$  and  $C_{13} = C_{12}$  for cubic crystal symmetry.

Equation (D.1) is used together with Eqs. (D.4) and (D.5) to compute the universal elastic anisotropy index  $A^u$ . Table D.6 lists the elastic constants  $C_{ij}$  and the calculated  $A^u$  of all the metals used in this study. In addition, the approximated value of  $A^u$ , denoted by  $\tilde{A}^u$ , is calculated as (see Eq. (6))

$$A^u \approx \tilde{A}^u = 6 \left( \frac{Y^V}{Y^R} - 1 \right) = 6 \left( \frac{K^V G^V (3K^R + G^R)}{K^R G^R (3K^V + G^V)} - 1 \right) \tag{D.6}$$

and compared to  $A^u$  in Tab. D.6. A good agreement is observed between  $A^u$  and  $\tilde{A}^u$  for all the materials studied. The corresponding error is found to be less than 15% with respect to the true  $A^u$ .

## Appendix E. Calculation of Taylor factor

Following the uniform strain assumption proposed by Taylor to estimate the stress-strain curve of a polycrystalline aggregate, Taylor factor is used to characterize the relation between local slips to the average strain

$$M_i = \frac{d\Gamma_i}{dE_{p,eq}} = \frac{\sum_{\alpha} d\gamma_i^{\alpha}}{dE_p}, \quad (\text{E.1})$$

where  $d\Gamma_i$  represents the increment of total accumulated slip in grain  $i$  and  $dE_{p,eq}$  is the increment of macroscopic equivalent (von Mises) plastic strain. For uniaxial loading, however,  $dE_{p,eq}$  reduces to the increment of macroscopic uniaxial plastic strain  $dE_p$ . The estimate for the equivalent (von Mises) grain stress  $\sigma_{i,eq}$  can be obtained from the equality requirement of plastic work increment on local and grain scales,

$$\sigma_{i,eq} dE_{p,eq} = \tau_0 d\Gamma_i, \quad \sigma_{i,eq} = M_i \tau_0, \quad (\text{E.2})$$

where identical critical resolved shear stress is assumed for all slip systems. Averaging the above relation leads to the classical estimate of yield stress in a polycrystalline aggregate under tension,  $\Sigma_y \approx \langle M \rangle \tau_0$ , where  $\langle M \rangle$  is the average Taylor factor.

For a given crystallographic orientation and equivalent plastic strain, Taylor factor can be computed using Eq. (E.1) by applying minimum work principle (or minimum microscopic shear principle) to get  $d\Gamma_i$ . This relies on linear programming, and dedicated tools are available in literature (see, *e.g.*, (Bachmann et al., 2010)). In order to obtain the distributions of Taylor factor in a polycrystalline aggregate for a specific macroscopic stress tensor, the associated equivalent plastic strain should be guessed to apply this methodology. In this study, an equivalent procedure has been used using Abaqus UMAT subroutine to calculate  $d\Gamma_i$ . The procedure is detailed below.

The macroscopic tensile loading is applied in  $X$  direction. In the model, the grains are assumed to be randomly oriented and described within crystal elasticity and ideal plasticity ( $H = 0$ ), accounting for different slip systems (FCC, BCC or HCPn). To obtain local accumulated slip ( $\Gamma_i$ ) and local stresses ( $\sigma^i$ ), the applied uniform total strain  $\mathbf{E} = \mathbf{e}^i$  is identified self-consistently as to recover the macroscopic uniaxial stress state of the model,  $\Sigma = \sum_i \sigma^i / N \approx \Sigma e_X \otimes e_X$ . When the number of grains  $N$  is large enough (*e.g.*,  $N \gtrsim 1000$ ) and grain orientations are randomly distributed (providing zero texture), the macroscopic response of the aggregate becomes quasi-isotropic. In this limit, the macroscopic uniaxial stress state is realized (approximately) when the applied total strain is of the form  $\mathbf{E} = E e_X \otimes e_X - \nu E (e_Y \otimes e_Y + e_Z \otimes e_Z)$ . To achieve self-consistency, hence, a macroscopic Poisson number  $\nu(E)$  needs to be determined as a function of total strain  $E$ . The optimal  $\nu(E)$  is selected when  $\Sigma$  becomes closest to the uniaxial stress solution  $\Sigma e_X \otimes e_X$ . In this respect, a code for the identification of  $\nu(E)$  was written, based on the minimization of  $\sum_{i,j} \Sigma_{ij}^2 - \Sigma_{11}^2$ , and coupled to UMAT subroutine for the calculation of local stresses  $\sigma^i$ . The UMAT subroutine followed the implementation of Huang (Huang, 1991) where slight modifications were needed to accommodate the shear flow law of Eq. (2). Once  $\nu(E)$  is determined,  $\Gamma_i$  follows immediately from the UMAT. It can be noted that the same Taylor factor is obtained for equibiaxial loading conditions due to the equivalence of applied macroscopic strains.

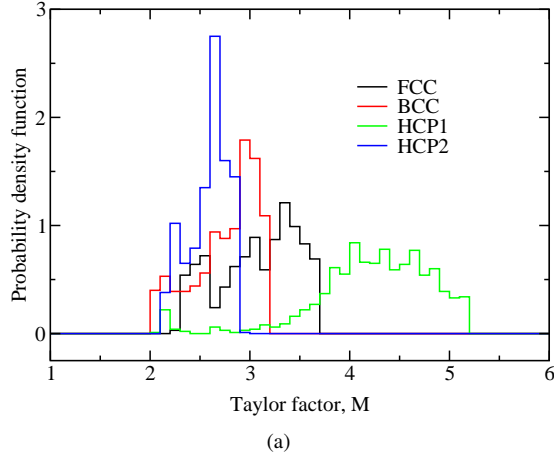


Figure E.21. Probability density function of Taylor factor calculated in a 1000-grain aggregate model with uniform strain assuming crystal elasticity and ideal plasticity with various slip systems under uniaxial (or equibiaxial) loading conditions. Results are shown for total strain of 0.05.

Figure E.21 shows the distributions of Taylor factor calculated in a uniform-strain polycrystal model with  $N = 1000$  grains and different slip systems: FCC, BCC, HCP1 and HCP2. Rather unusual, multi-modal distributions are observed which seem to be intrinsic to (random) aggregate model and not a statistical error (note that each distribution is composed of 1000 data points). However, the average Taylor factor,  $\langle M \rangle = \sum_i M_i / N$ , seems to be well correlated with the distribution width measured, *e.g.*, by its standard deviation,  $s(M) = \sqrt{\langle M^2 \rangle - \langle M \rangle^2}$ . Smaller  $\langle M \rangle$  implies also smaller  $s(M)$ . It is therefore reasonable to assume that distributions can be well characterized by first two statistical moments, see Tab. E.7.

Crystal system	$\langle M \rangle$	$s(M)$
FCC	3.07	0.391
BCC	2.76	0.320
HCP1	4.23	0.603
HCP2	2.58	0.197

Table E.7. Average Taylor factor,  $\langle M \rangle$ , and standard deviation of Taylor factor,  $s(M)$ , calculated in a 1000-grain aggregate model with uniform strain assuming crystal elasticity and ideal plasticity with various slip systems under uniaxial (or equibiaxial) loading conditions. Results are shown for total strain of 0.05.

The average Taylor factors for FCC and BCC may be compared with the values published in literature. In Tab. 1 of (Rosenberg and Piehler, 1971),  $\langle M \rangle = 3.067$  and 2.754 are found to be in excellent agreement with the values shown in Tab. E.7.

## References

- M.A. Arafin and J.A. Szpunar. A new understanding of intergranular stress corrosion cracking resistance of pipeline steel through grain boundary character and crystallographic texture studies. *Corrosion Science*, 51:119–128, 2009.
- F. Bachmann, R. Hielscher, and H Schaeben. Texture analysis with MTEX - free and open source software toolbox. *Solid State Phenomena*, 160:63–68, 2010.
- F. Barbe, S. Forest, and G. Cailletaud. Intergranular and intragranular behavior of polycrystalline aggregates. Part 1: F.E. model. *Int. J. Plasticity*, 17:513–536, 2001a.
- F. Barbe, S. Forest, and G. Cailletaud. Intergranular and intragranular behavior of polycrystalline aggregates. Part 2: Results. *Int. J. Plasticity*, 17:537–563, 2001b.
- J. Bassani and T. Y. Wu. Latent hardening in single crystals. II. analytical characterization and predictions. *Proceedings: Mathematical and Physical Sciences*, 435:21–41, 1991.
- C.D. Beachem. A new model for hydrogen-assisted cracking (hydrogen "embrittlement"). *Metallurgical Transactions*, 3:437–451, 1972.
- T.R. Bieler, P. Eisenlohr, F. Roters, D. Kumar, D.E. Mason, and M.A. Crimp. The role of heterogeneous deformation on damage nucleation at grain boundaries in single phase metals. *Int. J. Plasticity*, 25:1655–1683, 2009.
- A. F. Bower. *Applied Mechanics of Solids*. Taylor & Francis Group, 2010.
- T.D. Burleigh. The postulated mechanisms for stress corrosion cracking of aluminum alloys: A review of the literature 1980-1989. *Corrosion*, 47:89–98, 1991.
- G. Cailletaud. A micromechanical approach to inelastic behavior of metals. *Int. J. Plasticity*, 8:55–74, 1991.
- CEA. *Cast3M*, 2015. [www-cast3m.com](http://www-cast3m.com).
- T. Couvant. Prediction of igsc as a finite element modeling post-analysis. In *Proceedings of the 18th International Conference on Environmental Degradation of Materials in Nuclear Power Systems - Water Reactors*, 2018.
- T. Couvant, J. Proix, and A. Seyeux. Modeling intergranular stress corrosion cracking of austenitic alloys exposed to PWR primary water. In *European Corrosion Congress, ISBN:978-989-98850-0-4*, 2013.
- T. Couvant, J. Caballero, C. Duhamel, J. Crépin, and T. Maeguchi. Calibration of the local igsc engineering model for alloy 600. In *Proceedings of the 18th International Conference on Environmental Degradation of Materials in Nuclear Power Systems - Water Reactors*, 2018.
- B. Cox. Environmentally induced cracking of zirconium alloys. Technical report, Atomic Energy of Canada Limited, 1970.
- B. Cox. Environmentally-induced cracking of zirconium alloys - A review. *J. Nuc. Mat.*, 170:1–23, 1990.
- O. Diard, S. Leclercq, G. Rousselier, and G. Cailletaud. Distribution of normal stress at grain boundaries in multicrystals: Application to an intergranular damage modeling. *Comp. Mat. Sci.*, 25:73–84, 2002.

- O. Diard, S. Leclercq, G. Rousselier, and G. Cailletaud. Evaluation of finite element based analysis of 3D multicrystalline aggregates plasticity. Application to crystal plasticity model identification and the study of strain fields near grain boundaries. *Int. J. Plasticity*, 21:691–722, 2005.
- S. El Shawish and L. Cizelj. Combining single- and poly-crystalline measurements for identification of crystal plasticity parameters: Application to austenitic stainless steel. *Crystals*, 7:181–200, 2017.
- S. El Shawish, L. Cizelj, and I. Simonovski. Modeling grain boundaries in polycrystals using cohesive elements: qualitative and quantitative analysis. *Nuc. Eng. Des.*, 261:371–381, 2013.
- Z. Fan, Y. Wu, X. Zhao, and Y. Lu. Simulation of polycrystalline structure with Voronoi diagram in Laguerre geometry based on random closed packing of spheres. *Comp. Mat. Sci.*, 29:301–308, 2004.
- C.J. Gardner, B.L. Adams, J. Basinger, and D.T. Fullwood. EBSD-based continuum dislocation microscopy. *Int. J. Plasticity*, 26:1234–1247, 2010.
- D. Gonzalez, I. Simonovski, P.J. Withers, and J. Quinta da Fonseca. Modelling the effect of elastic and plastic anisotropies on stresses at grain boundaries. *Int. J. Plasticity*, 61:49–63, 2014.
- Y. Guo, D.M. Collins, E. Tarleton, F. Hofman, J. Tischler, W. Liu, R. Xu, and A.J. Wilkinson. Measurements of stress fields near a grain boundary: Exploring blocked arrays of dislocations in 3d. *Acta Mat.*, 96:229–236, 2015.
- J. Gupta, J. Hure, B. Tanguy, L. Laffont, M.C. Lafont, and E. Andrieu. Evaluation of stress corrosion cracking of irradiated 304 stainless steel in PWR environment using heavy ion irradiation. *J. Nuc. Mat.*, 476:82–92, 2016.
- X. Han. *Modélisation de la fragilisation due au gonflement dans les aciers inoxydables austénitiques irradiés*. PhD thesis, Ecole Nationale Supérieure des Mines de Paris, 2012.
- T. Helfer, B. Michel, J.M. Proix, M. Salvo, J. Sercombe, and M. Casella. Introducing the open-source MFront code generator: Application to mechanical behaviors and materials knowledge management within the PLEIADES fuel element modelling platform. *Comp. Math. With Appl.*, 70:994–1023, 2015.
- T. Hoc and S. Forest. Polycrystal modelling of IF-Ti steel under complex loading path. *Int. J. Plasticity*, 17: 65–85, 2001.
- Y. Huang. User-material subroutine incorporating single crystal plasticity in the abaqus finite element program. Technical report, Division of Applied Sciences, Harvard University, 1991.
- J. Hure, S. El Shawish, L. Cizelj, and B. Tanguy. Intergranular stress distributions in polycrystalline aggregates of irradiated stainless steel. *J. Nuc. Mat.*, 2016.
- W. B. Hutchinson and M. R Barnett. Effective values of critical resolved shear stress for slip in polycrystalline magnesium and other hcp metals. *Scripta Materialia*, 63:737–740, 2010.
- IAEA. Stress corrosion cracking in light water reactors: Good practices and lessons learned. NP-T-3.13, IAEA Nuclear Energy Series, 2011.
- A.K. Kanjarla, P. Van Houtte, and L. Delannay. Assessment of plastic heterogeneity in grain interaction models using crystal plasticity finite element method. *Int. J. Plasticity*, 26:1220–1233, 2010.

- A. King, G. Johnson, D. Engelberg, W. Ludwig, and J. Marrow. Observations of intergranular stress corrosion cracking in a grain-mapped polycrystal. *Science*, 321:382–385, 2008.
- B.C. Larson, W. Yang, G.E. Ice, J.D. Budai, and J.Z. Tischler. Three-dimensional X-ray structural microscopy with submicrometre resolution. *Nature*, 415:887–890, 2002.
- M. Le Millier, O. Calonne, J. Crépin, C. Duhamel, L. Fournier, F. Gaslain, E. Hériprié, O. Toader, Y. Vidalenc, and G. Was. Influence of strain localization on IASCC of proton irradiated 304L stainless steel in simulated PWR primary water. In *16th International Conference on Environmental Degradation of Materials in Nuclear Power Systems - Water Reactors*, 2013.
- R. A. Lebensohn, C. N. , Tomé, and P. Ponte Castañeda. Self-consistent modelling of the mechanical behaviour of viscoplastic polycrystals incorporating intragranular field fluctuations. *Philosophical Magazine*, 87:4287–4322, 2007.
- R.A. Lebensohn, A.K. Kanjarla, and P. Eisenlohr. An elasto-viscoplastic formulation based on fast fourier transforms for the prediction of micromechanical fields in polycrystalline materials. *Int. J. Plasticity*, 32-33:59–69, 2012.
- A. Mbiakop, A. Constantinescu, and K. Danas. An analytical model for porous single crystals with ellipsoidal voids. *J. Mech. Phys. Solids*, 84:436–467, 2015.
- M.D. McMurtrey, B. Cui, I. Robertson, D. Farkas, and G.S. Was. Mechanism of dislocation channel-induced irradiation assisted stress corrosion crack initiation in austenitic stainless steel. *Cur. Op. Solid State Mat. Sci.*, 19:305–314, 2015.
- A. Musienko and G. Cailletaud. Simulation of inter- and transgranular crack propagation in polycrystalline aggregates due to stress corrosion cracking. *Acta Mat.*, 57:3840–3855, 2009.
- R.C. Newman and C. Healey. Stability, validity, and sensitivity to input parameters of the slip-dissolution model for stress-corrosion cracking. *Corrosion Science*, 49:4040–4050, 2007.
- H. Nishioka, K. Fukuya, K. Fujii, and T. Torimaru. IASCC initiation in highly irradiated stainless steels under uniaxial constant load conditions. *J. Nuc. Sci. and Tech.*, 45:1072–1077, 2008.
- J. Panter, B. Viguier, J.M. Cloué, M. Foucault, P. Combrade, and E. Andrieu. Influence of oxide films on primary water stress corrosion cracking initiation of alloy 600. *J. Nuc. Mat.*, 348:213–221, 2006.
- R.N. Parkins. Predictive approaches to stress corrosion cracking failures. *Corrosion Science*, 20:147–166, 1980.
- D. Peirce, R. J. Asaro, and A. Needleman. Material rate dependence and localized deformation in crystalline solids. *Acta Metall.*, 30:1951–1976, 1983.
- S.I. Ranganathan and M. Ostaja-Starzewski. Universal elastic anisotropy index. *Phys. Rev. Lett.*, 101:055504, 2008.
- A. Reuss. Berechnung der fliehgrenze von mischkristallen auf grund der plastizittitsbedingung fiir einkristalle. *Z. angew. Math. Mech.*, 9:55, 1929.
- J. M. Rosenberg and H. R Piehler. Calculation of the Taylor factor and lattice rotations for bcc metals deforming by pencil glide. *Metallurgical Transactions*, 2:257–259, 1971.

- M. Sauzay. Cubic elasticity and stress distribution at the free surface of polycrystals. *Acta. Mat.*, 55:1193–1202, 2007.
- C.H. Shen and P.G. Shewmon. A mechanism for hydrogen-induced intergranular stress corrosion cracking in alloy 600. *Metall. Trans. A.*, 21A:1261–1271, 1990.
- I. Simonovski and L. Cizelj. Automatic parallel generation of finite element meshes for complex spatial structures. *Comp. Mat. Science*, 50:1606–1618, 2011.
- I. Simonovski and L. Cizelj. Cohesive zone modeling of intergranular cracking in polycrystalline aggregates. *Nuc. Eng. Design*, 2014.
- Simulia. *ABAQUS 6.14-2*, 2016.
- M.O. Speidel. Stress corrosion cracking of aluminum alloys. *Metallurgical and Materials Transactions A*, 6A:631–651, 1975.
- K.J. Stephenson and G.S. Was. Crack initiation behavior of neutron irradiated model and commercial stainless steels in high temperature water. *J. Nuc. Mat.*, 444:331–341, 2014.
- D. Tromans. Elastic anisotropy of hcp metal crystals and polycrystals. *International Journal of Research and Reviews in Applied Sciences*, 6:462–483, 2011.
- D. Van Rooyen. Review of the stress corrosion cracking of inconel 600. *Corrosion*, 31:327–337, 1975.
- W. Voigt. *Lehrbuch der Kristallphysik*. Teubner, 1928.
- Z.F. Wang and A. Atrens. Initiation of stress corrosion cracking for pipeline steels in a carbonate-bicarbonate solution. *Metallurgical and Materials Transactions A*, 27A:2686–2691, 1996.
- C. Zener. *Elasticity and Anelasticity of Metals*. University of Chicago, 1948.
- R. Zhou, E. A. West, Z. Jiao, and G. Was. Irradiation-assisted stress corrosion cracking of austenitic alloys in supercritical water. *J. Nuc. Mat.*, 395:11–22, 2009.